Sprenger, M., Seeger, S., Blume, T., Weiler, M. (2016): Travel times in the vadose zone: Variability in space and time. - *Water Resources Research*, *52*, pp. 5727—5754.

DOI: http://doi.org/10.1002/2015WR018077

AGU PUBLICATIONS

Water Resources Research

RESEARCH ARTICLE
10.1002/2015WR018077

Travel times in the vadose zone: Variability in space and time

Matthias Sprenger[1], Stefan Seeger[1], Theresa Blume[2], and Markus Weiler[1]

[1]Hydrology, Faculty of Environment and Natural Resources, University of Freiburg, Freiburg, Germany, [2]GFZ German Research Centre for Geosciences, Potsdam, Germany

Key Points:
- Seasonal effects produce multimodal patterns in travel time distributions
- Rainfall patterns control temporal and soil type spatial variation of travel times
- Unsaturated zone travel times are long compared to those observed at the catchment outlet

Correspondence to:
M. Sprenger,
matthias.sprenger@abdn.ac.uk

Citation:
Sprenger, M., S. Seeger, T. Blume, and M. Weiler (2016), Travel times in the vadose zone: Variability in space and time, *Water Resour. Res.*, *52*, 5727–5754, doi:10.1002/2015WR018077.

Received 7 SEP 2015
Accepted 28 MAY 2016
Accepted article online 3 JUN 2016
Published online 5 AUG 2016

Abstract Water travel times reflect hydrological processes, yet we know little about how travel times in the unsaturated zone vary with time. Using the soil physical model HYDRUS-1D, we derived time variable travel time distributions for 35 study sites within the Attert catchment in Luxembourg. While all sites experience similar climatic forcing, they differ with regard to soil types (16 Cambisols, 12 Arenosols, and 7 Stagnosols) and the vegetation cover (29 forest and 6 grassland). We estimated site specific water flow and transport parameters by fitting the model simulations to observed soil moisture time series and depth profiles of pore water stable isotopes. With the calibrated model, we tracked the water parcels introduced with each rainfall event over a period of several years. Our results show that the median travel time of water from the soil surface to depths down to 200 cm is mainly driven by the subsequent rainfall amounts. The median time until precipitation is taken up by roots is governed by the seasonality of evapotranspiration rates. The ratio between the amount of water that leaves the soil profile by on the one hand and evaporation and transpiration on the other hand also shows an annual cycle. This time variable response due to climatic forcing is furthermore visible in the multimodal nature of the site specific master transit time distribution representing the flow-averaged probability density for rainwater to become recharge. The spatial variability of travel times is mainly driven by soil texture and structure, with significant longer travel times for the clayey Stagnosols than for the loamy to sandy Cambisols and Arenosols.

1. Introduction

Water travel times are seen as a characteristic measure to reflect hydrological processes at the catchment [*McGuire and McDonnell*, 2006; *Rodhe et al*., 1996], hillslope [*McGuire*, 2007], or pedon scale [*Lindström and Rodhe*, 1992; *Stewart and McDonnell*, 1991]. However, it has been shown that the time variable character of the hydrological processes needs to be considered in travel time estimations [*Rinaldo et al*., 2011]. The variation of travel times can be explained by physical and meteorological controls that influence the catchment states and processes [*Birkel et al*., 2012; *Heidbüchel et al*., 2013; *Tetzlaff et al*., 2014; *van der Velde et al*., 2010]. Especially, assumptions about the mixing of water within the hydrological system were found to be crucial for the estimation of travel time distributions (TTD), which challenges the common well-mixed assumption [*Botter*, 2012; *Hrachowitz et al*., 2013; *Rinaldo et al*., 2015; *van der Velde et al*., 2012, 2015]. Therefore, conceptual models, where the vadose zone is explicitly represented in addition to the saturated zone (e.g., groundwater storage) are recently gaining popularity [*Birkel et al*., 2015; *Benettin et al*., 2015a, 2013b; *Kirchner*, 2016a; *Shaw et al*., 2008]. Changes in the size of the vadose zone storage [*McMillan et al*., 2012] and also from well-mixed to partially mixed conditions [*Hrachowitz et al*., 2013] were shown to have a high influence on the tails (shortest and longest travel times) of TTD. Especially the long travel times characterized in the tails of catchment TTD are generally difficult to assess with water stable isotope data [*Seeger and Weiler*, 2014], because the longer the transit times, the more damped the tracer input signal at the catchment outlet, leading to a low signal-to-noise ratio (tracer variation versus uncertainties). Further, focusing on the tracer signal at the catchment outlet gives limited insight into processes that take place within the catchment, since the catchment outlet is often highly influenced by near stream processes [*Kirchner et al*., 2001; *Sayama and McDonnell*, 2009; *Tetzlaff et al*., 2014]. For the catchment internal processes, the unsaturated (vadose) zone, where interaction between the groundwater and atmosphere takes place [*Hopmans and van Genuchten*, 2005], plays a crucial role, highly influencing the catchment travel times [*Botter et al*., 2010; *Rinaldo et al*., 2011]. In the vadose zone, rainfall input is partitioned into recharging and evapotranspiring water [*Botter*, 2012; *Queloz et al*., 2015a]. Routing of recharge to the stream can be delayed by years, while

the hydraulic pressure is transmitted rapidly [*McDonnell and Beven*, 2014; *Stewart et al*., 2007]. These vadose zone processes will vary over time, depending on the variable meteorological forcing, vegetation activity, and storage states [*Harman et al*., 2011].

Consequently, time variable TTD cannot be defined by constant parameters, as shown by comparisons between soil physical models and a lumped convolution approaches to simulate the solute breakthrough at the hillslope scale [*Ali et al*., 2014; *Rinaldo et al*., 2011]. However, an application of these concepts at the pedon scale is still lacking, despite the fact that dynamic modeling approaches have shown that a combination of mixing and piston flow assumptions is suitable to simulate temporal variations in travel times for a lysimeter [*Lindström and Rodhe*, 1992]. Instead, time invariant transfer functions, who were shown to be partly at odds due to the high degree of intermittency exhibited by the rainfall forcing [*Botter et al*., 2010], are still widely applied for the vadose zone, calibrated by the relation between the isotopic signal of the rainfall input and the pore water stable isotope variation at a certain soil depth [*Hu et al*., 2015; *Kabeya et al*., 2011; *Kim and Jung*, 2014; *Muñoz-Villers and McDonnell*, 2012; *Tetzlaff et al*., 2014; *Timbe et al*., 2014].

As lumped model approaches, where the spatial variations of parameters are ignored and the flow pattern is assumed to be constant [*Zuber and Małoszewski*, 2001], seem to oversimplify the soil-vegetation-atmosphere interactions it might be helpful to use soil physical models. To calibrate soil physical models, the isotopic signal of the outflow of lysimeters has been shown to allow for an inverse estimation of the dispersivity parameter, while water flow parameters have been fitted to soil moisture time series [*Stumpp et al*., 2009, 2012]. Since the isotopic composition of recharge is not easily sampled in the field, pore water stable isotope profiles have been used instead to calibrate the solute transport [*Adomako et al*., 2010; *Sprenger et al*., 2015b]. *Sprenger et al*. [2015b] showed that an inverse model procedure that considers both soil moisture and pore water stable isotope data in parallel, is suitable to derive soil hydraulic parameters that reflect the water balance. Furthermore, since the multiobjective calibration suggested by *Sprenger et al*. [2015b] considers both the water celerities and water velocities [*McDonnell and Beven*, 2014; *Rinaldo et al*., 2011], travel times can be directly derived by tracking the transport and dispersion of the input water (see *Harman and Kim* [2014] and *Benettin et al*. [2015b], for theoretical explanations on tracer injection experiments).

On the basis of the above outlined recent developments on catchment travel time modeling, we formulate our research questions as follows: How can we use a soil physical model to allow us to infer time variable travel times that can be related to the variable environmental conditions at 35 soil profiles? How variable are the travel times within the catchment and can the variability in space and time be explained by environmental characteristics? Thus, the objective of the present study is to first parameterize the soil physical model by fitting the simulation to observed soil moisture and pore water stable isotope data. Afterwards, we use the calibrated model to track the fate of water parcels introduced by the precipitation input. These simulations allow us to derive site specific time variable travel times of water leaving the soil profile by drainage or transpiration as well as characteristic flow-averaged TTD for comparative analysis.

2. Methods

2.1. Study Sites

The 35 study sites are distributed over the Attert catchment in the Grand Duchy of Luxembourg. The lithology of the Attert catchment is characterized by Devonian schist in the north, Jurassic Luxembourg sandstone in the south, and Triassic marls in between [*Colbach and Maquil*, 2003] (Figure 1). This geological setting results in three regions of different characteristics with regard to the soil type, topography, and land use.

The studied soils in the Schist area are haplic Cambisols (CM) [*IUSS Working Group WRB*, 2006] with a typical Ah-Bw-Cw horizonation. The thickness of these horizons is variable with a humified mineral horizon (Ah-horizon) of about 10–20 cm at forested sites and a 20–30 cm at grassland sites (Tables 1 and 2). While the A-horizon has a low stone content and a dark brownish color, there is an increase in stones over depth in the Bw-horizon and the color of the soil matrix is light brown. The slate rock fragments in the Bw-horizon are partially repositioned horizontally due to their origin in periglacial slope deposits [*Juilleret et al*., 2011]. In depths between 60 and 155 cm, the rock fragment content reaches 75%, which is defined as the Cw-horizon [*Wittmann et al*., 1997]. At the Bw-Cw-boundary, the horizontal repositioning slate rock fragments

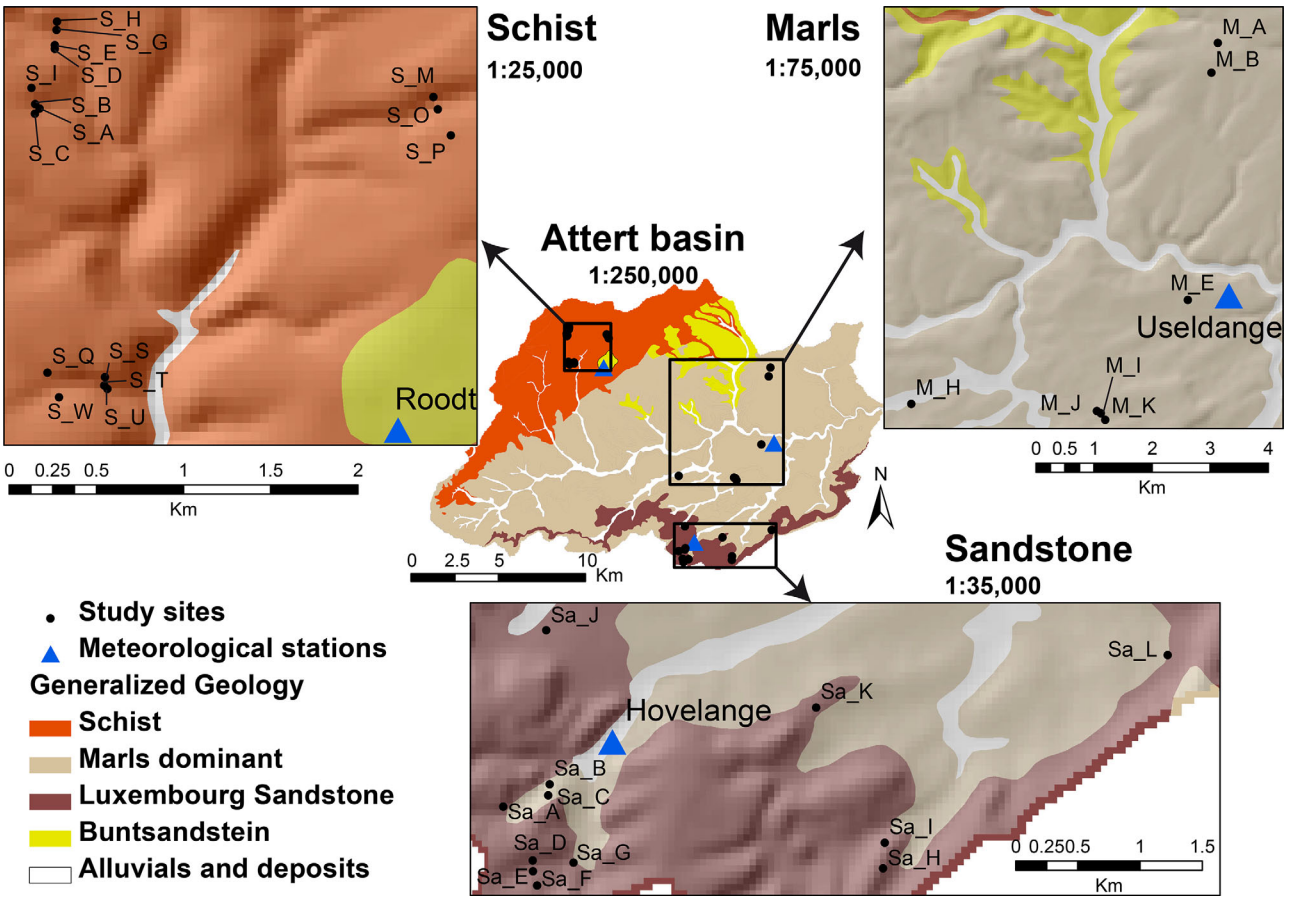

Figure 1. Location of the study sites and the meteorological stations within the Attert basin, grouped according to the geological settings. Note that the subplots have different scales.

changes into a more vertical alignment. The soil texture varies between loam, silty loam, and clayey loam with increasing clay content with depth. In conclusion, the Cambisols are freely draining to the depth at which the schist bedrock is reached.

At the study sites on Luxembourg sandstone, Arenosols (AR) [*IUSS Working Group WRB*, 2006] have developed [*Martínez-Carreras et al*., 2012]. They hold a relatively thin dark brown Ah-horizon (ca. 10 cm) below which heavily weathered ocher colored sandstone material follows. The soil texture ranges from sandy loam, sandy clay loam to loam. The stone content is generally low (<3%) and the unaltered parent sand stone is usually not reached within the first 200 cm below soil surface. Horizons within the upper 200 cm differ by textural variations due the parent material, which can result in banded layers of elevated clay content. The sandy Arenosols provide freely draining hydrological conditions resulting in deep percolation.

At the study sites on the marls substrata, Stagnosols (ST) [*IUSS Working Group WRB*, 2006] are present with a water draining horizon (Sw) below the Ah-horizon, followed by a more compact horizon (Sd) with redoximorphic properties [*Ad-hoc-Arbeitsgruppe Boden*, 2005; *Wittmann et al*., 1997]. The Stagnosols are rich in clay (20–60%) and have little sand content (7–20%), but higher sand contents can occur as banded layers in the soil profile (sand content of 30–50%). The rock content is generally low and the soil color is light gray and occasionally shifts toward red in the subsoil due to the parent material. The drainage potential of the Stagnosols is limited due to their fine textured matrix leading to low hydrological conductivities and low storage capacities for these soils.

The topography in the Attert catchment is determined by the geological setting, with steep slopes developed on the schist and sandstone, while the marls region is characterized by gently sloping terrain with

Table 1. Study Site Characteristics Regarding the Soil Type, Location, Altitude, Topography, Aspect, Slope, Land Use, Horizontation, and Dominant Texture of the Soils

Site ID	Soil Type	Latitude (WGS84)	Longitude (WGS84)	Altitude (m.a.s.l.)	Topographical Position	Aspect	Slope (°)	Land Use	Horizon 1	Horizon 2	Horizon 3	Dominant Soil Texture
S_A	CM	49.82255	5.80253	451	Footslope	E	12.0	Forest	Ah	Bw	Cw	Sandy clay loam
S_B	CM	49.82282	5.80219	462	Hillslope	SE	12.0	Forest	Ah	Bw	Cw	Silt loam
S_C	CM	49.82232	5.80245	464	Hillslope	NE	15.0	Forest	Ah	Bw	Cw	Sandy clay loam
S_D	CM	49.82568	5.80371	449	Hillslope	NE	14.2	Forest	Ah	Bw	Cw	Silt loam
S_E	CM	49.82587	5.80370	446	Hillslope	NE	11.7	Forest	Ah	Bw	Cw	Sandy clay loam
S_G	CM	49.82664	5.80385	446	Hillslope	S	19.3	Forest	Ah	Bw	Cw	Silt loam
S_H	CM	49.82710	5.80388	465	Hillslope	S	17.8	Forest	Ah	Bw	Cw	Silt loam
S_I	CM	49.82365	5.80190	480	Plateau		6.9	Grassland	Ap	Bw	Cw	Silt loam
S_M	CM	49.82327	5.83394	459	Hillslope	S	21.5	Forest	Ah	Bw	Cw	Silty clay
S_O	CM	49.82265	5.83429	450	Hillslope	N	14.6	Forest	Ah	Bw	Cw	Silt loam
S_P	CM	49.82130	5.83533	482	Plateau		6.0	Grassland	Ap	Bw	Cw	Silt loam
S_Q	CM	49.80898	5.80326	453	Slope	S	10.6	Pasture	Ap	Bw	Cw	Silt loam
S_S	CM	49.80875	5.80784	430	Hillslope	S	23.0	Forest	Ah	Bw	Cw	Sandy clay
S_T	CM	49.80831	5.80779	404	Hillslope	S	21.5	Forest	Ah	Bw	Cw	Sandy clay
S_U	CM	49.80814	5.80805	396	Footslope		8.0	Forest	Ah	Bw	Cw	Sandy clay
S_W	CM	49.80771	5.80418	443	Hillslope	N	15.2	Forest	Ah	Bw	Cw	Silt loam
Sa_A	AR	49.80651	5.96444	350	Hillslope	SE	16.0	Forest	Ah	BI	BII	Sand
Sa_B	AR	49.80188	5.96294	312	Footslope	NW	7.3	Forest	Ah	BI	BII	Sandy loam
Sa_C	AR	49.76667	5.95744	331	Hillslope	NW	16.8	Forest	Ah	BI	BII	Sand
Sa_D	AR	49.75049	5.89149	355	Hillslope	S	12.7	Forest	Ah	BI	BII	Sand
Sa_E	AR	49.74916	5.93679	342	Footslope		5.0	Forest	Ah	BI	BII	Loamy sand
Sa_F	AR	49.74956	5.93600	360	Hillslope	NE	13.8	Forest	Ah	BI	BII	Sand
Sa_G	AR	49.74799	5.93757	320	Footslope		2.9	Forest	Ah	BI	BII	Sandy loam
Sa_H	AR	49.82260	5.80253	345	Hillslope	E	13.0	Forest	Ah	BI	BII	Loamy sand
Sa_I	AR	49.71151	5.89190	322	Hillslope	N	20.3	Forest	Ah	BI	BII	Sand
Sa_J	AR	49.72464	5.89634	297	Plateau		2.3	Grassland	Ap	BI	BII	Loamy sand
Sa_K	AR	49.71235	5.89691	308	Plateau		3.5	Pasture	Ap	BI	BII	Loamy sand
Sa_L	AR	49.70764	5.89522	298	Plateau		6.2	Grassland	Ap	BI	BII	
M_A	ST	49.70686	5.89526	365	Plateau		1.8	Forest	Ah	Sw	Sd	Silty clay
M_B	ST	49.70583	5.89572	360	Plateau		4.1	Forest	Ah	Sw	Sd	Sandy clay
M_E	ST	49.70749	5.89979	260	Plateau		2.0	Grassland	Ap	Sw	Sd	Clay
M_H	ST	49.70717	5.93422	270	Plateau		5.4	Grassland	Ap	Sw	Sd	Clay loam
M_I	ST	49.70898	5.93443	286	Footslope		4.0	Forest	Ah	Sw	Sd	Silty clay
M_J	ST	49.71874	5.92673	280	Footslope		3.8	Forest	Ah	Sw	Sd	Clay
M_K	ST	49.72439	5.96730	280	Footslope		1.1	Forest	Ah	Sw	Sd	Silty clay

wide valleys. The land use on the CM in the schist area is dominated by forests on the steep slopes, while most plateaus and floodplains are pasture and arable land. Forested slopes also dominate on the AR in the sandstone area, while the marl region is more dominated by grassland and agriculture. However, since we excluded areas influenced by groundwater, the remaining ST sites are mainly forested.

Of the 35 study sites, 16 are located in the schist, 12 in the sandstone, and 7 in the marls region (Figure 1). Site specific characteristics such as soil type, location, altitude (DEM 5 m), topographical position, aspect, slope, land use, delineated soil horizons, and dominant soil texture are summarized in Table 1. The forested sites are all deciduous woods dominated by beech (*Fagus sylvatica*); but oak (*Quercus robu*) and maple (*Acer pseudoplatanus*) trees are also present. The grassland sites are generally used as pasture or meadow.

Since the distance between the different study sites is no more than 20 km, the atmospheric conditions are similar, as shown by the meteorological data of three meteorological stations from the administration des services techniques de l'agriculture de Luxembourg (ASTA) close to Roodt, Huwelange, and Useldange, representing the schist, sandstone, and marls, respectively (Figure 1): the average annual precipitation sum did not differ significantly (Kruskal-Wallis test, $\chi^2 = 0.475$, $p = 0.79$) between 2007 and 2013 with 825, 777, and 784 mm for Roodt, Hovelange, and Useldange. The temporal dynamics of rainfall are also similar, since the daily precipitation data correlate linearly significantly with each other ($r > 0.81$; $p < 0.01$). The annual average air temperatures between 2007 and 2013 for Roodt, and Hovelange, are similar with 8.4 and 8.5°C. However, according to a Kruskal-Wallis test with a posthoc test after Tukey and Kramer (Nemenyi), the air temperature in Useldange is with 9.9°C significantly ($p < 0.01$) higher than at the other two meteorological stations.

Table 2. Boundaries Between the Three Horizons (H1, H2, H3), Lower Boundary of the Parameter Range of θ_s, min., and max. LAI of the Vegetation, Maximum Observed Rooting Depth, Average Air Temperature, and Dates of the Isotope Profile Sampling and the Start of the Soil Moisture Measurements

Site ID	Boundary H1 to H2 (cm)	Boundary H2 to H3 (cm)	Lower Boundary θ_s ($cm^3\ cm^{-3}$)	min. LAI ($m^2\ m^{-2}$)	max. LAI ($m^2\ m^{-2}$)	max. Rooting Depth (cm)	Average air Temperature (°C)	Isotope Profile Sampling Dates		Start Soil Moisture
S_A	15	155	0.50	1.34	6.57	69	8.3	25 Feb 2012	2 Jun 2014	29 Feb 2012
S_B	11	100	0.42	1.10	6.74	63	7.8	26 Feb 2012	2 Jun 2014	11 May 2012
S_C	11	138	0.48	1.18	6.67	78	8.3	28 Feb 2012	2 Jun 2014	11 May 2012
S_D	11	151	0.41	2.40	6.70	69	8.3	28 Mar 2012	2 Jun 2014	11 Apr 2012
S_E	14	98	0.45	1.80	6.74	86	8.1	27 Mar 2012	2 Jun 2014	11 Apr 2012
S_G	11	104	0.42	1.07	6.46	46	8.1	28 Mar 2012	2 Jun 2014	30 Mar 2012
S_H	13	104	0.48	0.78	6.13	42	8.8	28 Mar 2012	2 Jun 2014	11 Apr 2012
S_I	27	63	0.46	1.00	3.80	35	8.6	30 Mar 2012	5 Jun 2014	30 Mar 2012
S_M	22	78	0.40	2.17	4.36	81	8.2	5 Jun 2012	4 Jun 2014	13 Jun 2012
S_O	21	97	0.43	1.39	4.07	107	7.9	20 Mar 2013	5 Jun 2014	20 Mar 2013
S_P	25	90	0.35	1.00	3.80	34	8.4	15 Oct 2013	4 Jun 2014	20 Mar 2013
S_Q	25	109	0.42	1.00	3.80	46	8.3	9 Jun 2012	3 Jun 2014	12 Jun 2012
S_S	20	84	0.42	2.01	5.66	80	8.6	14 Aug 2012	3 Jun 2014	18 Aug 2012
S_T	20	81	0.36	2.77	6.78	74	8.0	14 Aug 2012	3 Jun 2014	17 Aug 2012
S_U	21	75	0.45	2.96	5.77	76	8.0	15 Aug 2012	3 Jun 2014	17 Aug 2012
S_W	14	95	0.33	1.73	6.07	84	8.7	15 Mar 2013	6 Jun 2014	19 Mar 2013
Sa_A	13	92	0.42	1.98	4.74	104	8.9	13 May 2013	11 Jun 2014	16 May 2013
Sa_B	11	44	0.45	1.19	4.74	97	8.6	21 Mar 2013	11 Jun 2014	21 Mar 2013
Sa_C	12	66	0.48	1.46	4.74	115	8.3	21 Mar 2013	11 Jun 2014	21 Mar 2013
Sa_D	11	110	0.40	1.48	4.95	81	8.3	19 Sep 2013	11 Jun 2014	19 Sep 2013
Sa_E	11	120	0.43	1.92	4.35	106	8.3	19 Sep 2013	11 Jun 2014	18 Sep 2013
Sa_F	11	125	0.42	1.65	4.93	63	8.0	19 Sep 2013	10 Jun 2014	19 Sep 2013
Sa_G	11	110	0.48	1.22	4.74	107	8.1	15 Aug 2013	10 Jun 2014	15 Aug 2013
Sa_H	11	92	0.43	0.86	4.74	93	8.6	24 Jul 2013	11 Jun 2014	24 Jul 2013
Sa_I	11	100	0.32	0.66	4.74	120	8.7	23 Jul 2013	11 Jun 2014	23 Jul 2013
Sa_J	20	130	0.42	1.00	3.80	33	8.8	26 Jul 2013	6 Jun 2014	25 Jul 2013
Sa_K	15	87	0.41	1.00	3.80	101	8.8	6 Sep 2013	6 Jun 2014	15 Sep 2013
Sa_L	28	120	0.45	1.00	3.80	29	9.0	21 Sep 2013	6 Jun 2014	21 Sep 2013
M_A	11	48	0.42	1.02	4.56	82	9.5	21 Mar 2013	12 Jun 2014	20 Mar 2013
M_B	11	40	0.50	1.05	5.10	82	9.4	21 Mar 2013	12 Jun 2014	21 Mar 2013
M_E	15	48	0.50	1.00	3.80	37	10.0	17 Sep 2013	11 Jun 2014	17 Sep 2013
M_H	17	66	0.45	1.00	3.80	39	9.2	14 Oct 2013	11 Jun 2014	18 Oct 2013
M_I	14	43	0.40	0.83	4.43	87	9.5	14 May 2013	12 Jun 2014	16 May 2013
M_J	17	53	0.45	1.43	5.44	99	9.6	15 May 2013	12 Jun 2014	7 Jun 2013
M_K	13	36	0.40	1.28	5.69	99	9.4	14 Oct 2013	12 Jun 2014	16 May 2013

2.2. Data Acquisition

2.2.1. Meteorological Data

In addition to the above mentioned temperature and precipitation measurements by the agricultural service of Luxembourg, the air temperature is measured at each of the 35 study sites using a Campbell Scientific CS215 probe. These shorter site specific time series (see Table 2) were extrapolated by multiple linear regressions between the daily mean, maximum, and minimum temperature at each study site and the long time series of the nearest meteorological station. Since the rainfall distribution is less variable over space, the daily rainfall sums at the meteorological stations closest to each study site were used. Rainfall was sampled for stable isotope analyses by the Luxembourg Institute of Science and Technology at least every 2 weeks in the schist region since November 2009. Additionally, isotope data for rainfall at the three meteorological stations in the different geological regions were available for the period between July 2012 and July 2013. The parallel rainfall sampling in the three geological settings showed that the fortnightly samples did not differ significantly (according to an Kruskal-Wallis test, $\chi^2 = 9.447$, $p = 0.008$), and correlated strongly with each other ($r > 0.98$, $p < 0.01$). In addition to the fortnightly sampling, event based rainfall samples in 4 mm intervals were taken in the schist region since July 2012. The isotopic composition of rainfall was determined with a wavelength-scanned cavity ring down spectrometer (WS-CRDS, Picarro, Santa Clara, USA) at the Luxembourg Institute of Science and Technology (fortnightly samples) and at the University of Freiburg (event based samples). For the period between 2001 and November 2009, monthly isotopic compositions of rainfall in the Attert Catchment were estimated via interpolation of values measured at surrounding GNIP stations (Beek, De Bilt, Emmerich, Groningen, Karlsruhe, Koblenz, Orlean la Source, Stuttgart, Trier, Wasserkuppe Roehn, Wieringerwerf, Würzburg), using the procedure described in *Seeger and Weiler* [2014].

2.2.2. Soil Data

Soil moisture as the volumetric water content θ [%] was continuously measured in 5 min intervals in three soil profiles at each study site. These soil moisture profiles were within a distance of 8 m from each other and consisted of three sensors (5TE, Decagon, Pullman, USA, accuracy $\pm$3%) installed at 10, 30, and 50 cm depth. The installation dates of the sensors are listed in Table 2. Since the soil moisture sensors were not calibrated, the time series for each depth were bias corrected as follows:

$$\theta'_n(t) = \theta_n(t) - (\overline{\theta}_n - \overline{\theta_{nmk}}), \quad (1)$$

where $\theta'_n(t)$ is the bias corrected soil moisture time series at replicate n, $\theta_n(t)$ is the raw time series, and $\overline{\theta}_n$ and $\overline{\theta_{nmk}}$ are the average of the soil moisture time series at replicate n and all three replicates (nmk), respectively.

For each study site and depth, the mean daily soil moisture was calculated with the bias corrected time series (usually with a sample size of $n = 3$, in case of sensor failures: $n = 2$).

Pore water stable isotope profiles were sampled twice at each study site within a radius of 5 m from the soil moisture profiles: once between February 2012 and October 2013 and once in June 2014 (Table 2). For the isotope profile sampling, soil cores of 8 cm diameter were taken with a percussion drill (Atlas Copco Cobra, Stockholm, Sweden). The soil cores were divided into subsamples of 5–10 cm length and the material was sealed in air tight bags (Weber Packaging, Güglingen, Germany). The pore water stable isotope analysis was conducted according to the direct equilibration method [*Garvelmann et al*., 2012; *Wassenaar et al*., 2008]. In the laboratory at the University Freiburg, dry air was added into the bags that were heat-sealed afterward and stored about 48 h at 21°C. After 2 days of equilibration between the pore water and the head space, the water saturated atmosphere in the bag was directly sampled with a needle connected to a WS-CRDS. After 4 min of sampling the headspace, a constant water vapor concentration was reached in the cavity at a value between 24,000 and 33,000 ppm. The average δ^{18}O and δ^{2}H measured during the subsequent 2 min at constant water vapor concentration were converted to values for the liquid phase by the temperature dependent fractionation factor according to *Majoube* [1971]. The calibration with the standard waters resulted in pore water stable isotope composition of the soil samples in ‰ relative to the VSMOW. These standards consisted of 10 mL of water with known isotopic composition of sea water ($\delta^{18}O = -0.4 \pm 0.2$‰, $\delta^{2}H = -2.7 \pm 1$‰), tap water ($\delta^{18}O = -9.5 \pm 0.2$‰, $\delta^{2}H = -64.5 \pm 1$‰), and snow water ($\delta^{18}O = -16.7 \pm 0.2$‰, $\delta^{2}H = -125.2 \pm 1$‰) to provide a sufficient range from heavy to light waters for the calibration. The mean standard deviation (SD) of these mean values were 0.31‰ for δ^{18}O and 1.16‰ for δ^{2}H at a SD of $<$100 ppm for the water vapor concentration. The applied direct equilibration method samples the resident concentration of the pore water stable isotope ratio, while transit time studies using lumped model approaches utilize the information about the mobile water sampled with suction lysimeter or wick samplers [*Sprenger et al*., 2015a]. However, in our simulations, the resident concentration is simulated and hence, also the resident concentration is the required data for the calibration procedure. An overview of the different methods to sample the isotopic composition of the pore water is given by *Sprenger et al*. [2015a], where the benefits and limitations are discussed. They further compared for split soil samples the stable isotopic composition derived with the direct equilibration and the widely used cryogenic extraction. The comparison of the two methods by *Sprenger et al*. [2015a] did not result in congruent isotope ratios. However, it is difficult to assess, which method provides the true pore water stable isotope data, since there is not standardized test available to validate the methods [*Orlowski et al*., 2016; *Sprenger et al*., 2015a]. However, the direct equilibration method, as used in the present study, seems to sample both mobile and immobile water, while hygroscopic and biologically bound water is not mobilized, as no heat is applied [*Sprenger et al*., 2015a].

For the first pore water stable isotope sampling (2012/2013), two profiles were taken at each study site. To compare the similarity of the two δ^{2}H-profiles, we calculated the mean absolute error (MAE) as the average differences of all sample pairs taken at the same depth ($\pm$2.5 cm). Since not only the absolute difference between the depths, but also the correlation between the depths is important, also the Kling-Gupta Efficiency KGE (as defined in equation (5), where KGE = 1 indicates that the two data sets are equal) was calculated for the two profiles at each study site. The MAE and KGE correlate significantly ($\rho = -0.45$). Generally, the MAE is on average 5.32‰ for δ^{2}H at the study sites and the KGE was on average 0.55, while the correlation coefficient was on average 0.76, the bias ratio 1.02, and the variability ratio 1.11. Of the two isotope profiles, the profile which reached greater depth or contained more data points was used for the inverse modeling approach.

Table 3. Overview of the Four-States Represented by the Phenologic Model to Simulate LAI Values for the Forested Sites

Model State	T_C Value	Required Condition to Enter Next State
I (fall)	Low → high	T_C reaches T_{Chigh}
II (winter)	High	GDD reach GDD_t
III (spring)	High → low	T_C reaches T_{Clow}
IV (summer)	Low	S_P reaches S_{Pt}

2.2.3. Vegetation Data

The maximum rooting depth of the vegetation was recorded during the soil sampling and an average site specific value was determined (Table 2).

The leaf area index (LAI) was measured with a LAI-2200 at several grasslands in the study area in July, August, and September 2013. These data and reported values for European grasslands by *Vuichard et al.* [2007] were used to derive monthly variable LAI-values, with a LAI_{min} between November and March of 1 m^2 m^{-2} [*Vuichard et al.*, 2007], a LAI_{max} during summer (June–August) of 3.8 m^2 m^{-2}, and a linear interpolation in the transition time [*Vuichard et al.*, 2007]. For the forested sites, the LAI was measured at each site once foliated and once defoliated (Table 2) with a LAI-2200.

In order to derive time variable LAI values for forested sites from this limited number of measurements, we used continuous solar radiation (R_S) measurements beneath the canopy, obtained by pyranometers (SP-212 Apogee, Logan, USA) installed at 2 m height at every study site. The ratio between R_S values measured on-site (beneath the canopy) and the R_S values of an open field reference site, was used to derive daily canopy transmittance (T_C) for each forest site. A four-state phenologic model based on *Wang et al.* [2004] was implemented to simulate the temporal succession of T_C values (see Table 3). During the model's autumn state, the modeled T_C value rises (at a rate controlled by a parameter e_a) from the low summer value T_{Clow} to the high winter value T_{Chigh}. The model's state transition from winter to spring occurs when the growing degree days (D_{GD}), which are the cumulative sum of all daily mean air temperatures above a base mean air temperature (D_{GDbase}) since a certain day of the year ($D_{GDstart}$), reach a certain threshold value D_{GDt}. In the model's spring state, the T_C value drops with a rate controlled by a parameter e_S, until it reaches the value T_{Clow}, where the model switches into the summer state. The transition from the summer state to the autumn state is triggered when the auxiliary senescence proxy S_P falls below a certain threshold S_{Pt}. In our case, S_P was computed according to equation (2), as a combination of 20 day moving average daily minimum air temperatures (T_{min20}) and the potential daily mean solar insolation (R_{Spot}) in W m^{-2}:

$$S_P = \sqrt{T_{\min 20}} * R_{Spot}, \tag{2}$$

The outlined four-state phenologic model has eight parameters: T_{Chigh}, T_{Clow}, D_{GDbase}, $D_{GDstart}$, D_{GDt}, e_s, e_a, and S_{Pt}. While the parameters T_{Chigh} and T_{Clow} could easily be set to the plateau values observed in the T_C time series, the remaining six parameters had to be optimized for each forest site. Apart from considerable noise during the winter time, the resulting time series of T_C values were suited to identify the completely foliated and defoliated periods as well as the transition phases and could thus be used to derive continuous LAI time series for each study site. Finally, the modeled continuous T_C time series could be used to infer continuous LAI time series from only two actual LAI measurements, by assuming an inverse relation between LAI and T_C.

2.3. Soil Physical Model

2.3.1. Water Flow

We used the soil physical model HYDRUS-1D [*Šimůnek et al.*, 2012] to estimate water flow and travel time through the vadose zone. A detailed description of the model setup and the parameterization is presented in *Sprenger et al.* [2015b], and the following sections will provide only a brief overview.

The transient water flow was simulated by numerically solving the Richards Equation according to the Mualem-van Genuchten model [*van Genuchten*, 1980]. The required water retention function $\Theta(h)$ and unsaturated conductivity function $K(h)$ were parameterized with the following Mualem-van Genuchten (MvG) parameters: residual volumetric water content θ_r [L^3 L^{-3}], saturated volumetric water content θ_s [L^3 L^{-3}], the inverse of the capillary fringe thickness α [L^{-1}], two shape parameters n [–], and m [–], where $m = 1 - 1/n$, the saturated hydraulic conductivity K_s [L T^{-1}], and a tortuosity parameter l [–]. The root water uptake was accounted for by a sink term in the Richards Equation according to *Feddes et al.* [1978]. The required matric potentials, that describe the optimal pressure head range for the root water uptake (−25 to −800 cm) and the thresholds at which oxygen stress (>−10 cm) or water stress (<−8000 cm) impedes

water uptake were taken from *Wesseling* [1991]. The rooting zone was defined by the observed site specific maximum rooting depth and the root distribution was defined in accordance to *Hoffman and van Genuchten* [1983] assuming the highest root density in the topsoil and an exponential decrease with depth, which is in line with field data gathered in broadleaved forests in Central Europe [*Meinen et al*., 2009].

The air temperature measurements at each study site and their temporal extrapolation via multiple regression were used to estimate site specific potential evapotranspiration (PET) according to the Hargreaves Formula. The generated time series of LAI were used to divide the potential evapotranspiration ET_p into potential evaporation E_p and potential transpiration T_p as [*Šimůnek et al*., 2012]:

$$E_p = ET_p e^{-0.463*\mathrm{LAI}}; T_p = ET_p(1-e^{-0.463*\mathrm{LAI}}). \quad (3)$$

The assumption that root water uptake (i.e., the sap flow) is directly related to the evaporation was shown to be true for beech in Central Europe [*Schwärzel et al*., 2009]. The LAI was further used to estimate dynamically the interception storage I as:

$$I = a * \mathrm{LAI}(t) * \left(1 - \frac{1}{1+\frac{C*P}{a*\mathrm{LAI}(t)}}\right), \quad (4)$$

with a being the empirical constant interception capacity of 0.55 mm; C the surface cover fraction as a function of the leaf area index LAI; and P the rainfall amount [*Šimůnek et al*., 2012]. Snow accumulation and its melting process were incorporated via the degree-day approach [*Jarvis*, 1994] with 4.3 mm d^{-1} K^{-1} as the empirical melting coefficient as suggested by *Šimůnek et al*. [2012].

2.3.2. Water Transport

We applied the advection dispersion equation to first simulate the transport of δ^2H through the soil profile in order to calibrate the soil physical model by inverse modeling and then trace the water molecules through the vadose zone to derive travel times. The parameters to describe advection and dispersion are the longitudinal dispersivity parameter λ [L], the molecular diffusion coefficient in free water D_w [L^2 T^{-1}] (2.272×10^{-9} m^2 s^{-1} according to *Mills* [1973]), and a tortuosity factor τ_w [–] as defined by *Millington and Quirk* [1961]. Since no fractionation effects occur during root water uptake [*Allison et al*., 1984; *Bariac et al*., 1990; *Zimmermann et al*., 1967], the water leaving the soil profile via transpiration influences the amount of water, but not its isotopic composition. Since the original HYDRUS code considers that the concentration of solutes (e.g., Br^-) increases during evaporation at the upper boundary layer, a modified version of the HYDRUS code published by *Stumpp et al*. [2012] was used. In the modified code, δ^2H leaves the soil domain with the evaporated water, leading to no changes in the pore water tracer concentration. Pore water stable isotope data taken in the field indicate that the fractionation effect is limited to the pore water in the uppermost 20 cm and thus evaporation fractionation [*Craig et al*., 1963] is neglected in the model, as it mostly influences ^{18}O composition anyway. The fact that the evaporation fractionation signal of the topsoil is not passed toward the percolating water has been shown in a global analysis of the isotopic composition of soil water, stream water, and groundwater [*Evaristo et al*., 2015]. As the fractionation signal is thus limited to the top 30 cm of the unsaturated zone (M. Sprenger et al., Illuminating hydrological processes in the vadose zone with pore water stable isotopes, submitted to *Reviews in Geophysics*, 2016), we neglected fractionation in our simulations. To ensure that the soil water affected by evaporation fractionation does not bias the model parameterization, we excluded the pore water isotope data of the upper 20 cm for the inverse model approach (see below).

2.3.3. Model Setup

The upper boundary condition of the water flow was defined as an atmospheric boundary condition with surface runoff and for the lower boundary free drainage (zero-gradient) was assumed. The boundary conditions with regard to water transport were defined as flow concentrations. For the initial conditions, the soil moisture was set to 30% and the pore water δ^2H was defined as $-54‰$ in accordance to the weighted mean in the precipitation. However, the influence of the initial conditions is assumed to be low, since a spin-up period of 5 years was applied for the inverse modeling. The δ^2H values were transformed to positive values for the calculations by adding an offset. For all study sites, the depth of the soil profiles was set to 200 cm and discretized into 101 nodes with higher resolution at the top than at the bottom of the profile. The profiles were divided into three different horizons according to the field observations (Tables 1 and 2).

Table 4. Boundaries of the Parameter Space for the Calibration by Inverse Modeling

Parameter	Lower Boundary	Upper Boundary
Residual volumetric water content, θ_r ($cm^3\ cm^{-3}$)	Const. 0.05	Const. 0.05
Saturated volumetric water content, θ_s ($cm^3\ cm^{-3}$)	Variable (VWC_{max}) for first and second horizon; 0.3 for the third horizon	0.6
inverse of the capillary fringe thickness, α (cm^{-1})	0.001	0.1
MVG shape parameter, n (–)	1.01	2.3
Saturated hydraulic conductivity, K_s (cm d^{-1})	10	1000
Tortuosity parameter l (–)	Const. 0.5	Const. 0.5
Longitudinal dispersivity, λ (cm)	0	30

2.3.4. Model Parameterization

The model was parameterized by inverse modeling on a daily resolution using simultaneously the soil moisture time series and the isotope profiles as a fitting target. The length of the soil moisture time series ranged between 430 and 998 days, depending on installation date. The sampling times of the isotope profiles are listed in Table 2. This multiobjective approach was shown to be a time efficient calibration procedure resulting in a good representation of the water flow and isotope transport [*Sprenger et al*., 2015b].

To reduce the number of free parameters for the site specific parameterization of the MvG model, θ_r was set constant to 5 vol %, since this value is reported for silty to sandy loam and silty clays [*Wessolek et al*., 2009] and the tortuosity parameter l was held constant at 0.5 in accordance to [*Mualem*, 1976]. For the MvG parameters, *Mertens et al*. [2006] and *Vrugt et al*. [2001] showed that θ_r is the least sensitive parameter when calibrating by inverse model approaches. *Vrugt et al*. [2001] further found a correlation of θ_r with the parameter n [*Vrugt et al*., 2001]. Consequently, it is not unusual that θ_r is kept constant [e.g., *Qu et al*., 2015, *Raviv et al*., 2008; *Vereecken et al*., 2007]. The best combinations of the remaining parameters θ_s, α, n, and K_s were searched by an inverse modeling procedure within the boundaries of the parameter space as listed in Table 4. One exception was the lower boundary of the θ_s-range for the first and second horizons, in which soil moisture data were available. For these horizons, the highest observed volumetric water content in the time series defined the lower boundary, while for the third horizon the lower boundary was fixed at 30 vol %. Simultaneously, the longitudinal dispersivity parameter λ was optimized in the parameter range 0–30 cm, which covers the range of λ as reported in the review by *Vanderborght and Vereecken* [2007]. Each soil horizon is represented by its individual parameter combination, but to reduce the number of parameters, a single value of λ was calibrated over the entire profile and for the horizons 2 and 3, the values for α and n were coupled. Thus, 11 parameters were calibrated for each study site to describe their soil hydraulic and transport properties.

The objective function for the inverse model procedure was based on the Kling-Gupta-Efficiency (KGE) [*Kling et al*., 2012]:

$$KGE = 1 - \sqrt{(r-1)^2 + (\beta-1)^2 + (\gamma-1)^2}, \tag{5}$$

where the observed and simulated data are compared with regard to the Pearson correlation (r), the ratio between the averages (bias ratio, $\beta = \mu_{sim}/\mu_{obs}$), and the ratio of the coefficients of variation (variability ratio, $\gamma = (\sigma_{sim}/\mu_{sim})/(\mu_{obs}/\sigma_{obs})$). In order to take simultaneously the soil moisture dynamics ($KGE_{\theta i}$) in the depths (i) of 10, 30, and 50 cm and the two δ^2H profiles (KGE_D) into account, a multiobjective Function (KGE_{mo}) was defined as:

$$KGE_{mo} = \frac{1}{3}\left[KGE_{\theta 10}\frac{N_{10}}{\sum N_i} + \frac{1}{2}\left(KGE_{\theta 30}\frac{N_{30}}{\sum N_i} + KGE_{\theta 50}\frac{N_{50}}{\sum N_i}\right) + \frac{1}{2}\left(KGE'_{D1} + KGE'_{D2}\right)\right], \tag{6}$$

where the $KGE_{\theta i}$ (as described in equation (5)) are weighted by the number of data points in the soil moisture time series (N_i) and the KGE'_D is a modified KGE-statistic for the isotope profiles that does not consider the bias ratio β. Excluding the comparison of the mean values between observed and simulated isotope profiles lowers the impact of errors of the absolute values of δ^2H in the precipitation input data, potentially introduced by interception leading to a site specific isotopic offset. Furthermore, the upper 15 cm of the isotope profiles were disregarded in the KGE'_D, because of the potential of evaporation fractionation in the topsoil, which is not implemented in the model. In addition, a possible influence of organic material, which

can absorb the wave lengths that are used for the stable water isotope analyses if they enter the cavity of the WS-CRDS [Brand et al., 2009; West et al., 2010], can be neglected by discarding the data from the humous top soil. Note that the soil moisture time series in 10 cm depth was weighted with a factor of 2 in the KGE_{mo} (equation (6)) to account for the important role of the topsoil for infiltration and evapotranspiration.

As optimization algorithm, we used the Lévy-Flight Krill Herd (LKH) algorithm, which was shown to outperform other the optimization algorithms with regard to the efficiency of the convergence [*Gandomi and Alavi*, 2012; *Wang et al*., 2013; *Gandomi and Alavi*, 2016]. With 500 krill (= parameter sets) in the herd moving in accordance to the swarm density (= parameter distribution), the food location (= center of mass for the objective function value), random diffusion and a local Lévy-flight operator over 10 iterations to a global optimum. Since some parameter combinations do not lead to a numerical convergence of the HYDRUS calculations during the optimization procedure, the LKH algorithm was modified: Krill representing such a nonconverging parameter combination were assigned their parameter combination of the previous iteration step. In the subsequent iteration, the krill would take a new direction, representing a new parameter set.

2.4. Travel Time Estimations

The vadose zone travel times for each study site were estimated in virtual tracer injection experiments [*Benettin et al*., 2015b] leading to probability density functions of travel times conditional on a given injection time [*Rinaldo et al*., 2011]. Travel time estimations were done for each day with precipitation that eventually passed the root zone and reached the 200 cm depth plane, which we define in accordance to *Hopmans and van Genuchten* [2005] as "recharge." The infiltrating rainwater parcel was labeled with a virtual ideal tracer [*Weiler and McDonnell*, 2004] and its fate in the soil was simulated using the parameter set that resulted in the highest KGE_{mo} for the particular soil profile. The mass flux of the virtual tracer normalized by the tracer mass input (M_{out}/M_{in}) was determined for each time step at −10, −30, −50, −100, −150, and −200 cm soil depth, as visualized exemplary for one depth in Figure 2 for one event in winter and one event in summer. Thus, the tracer mass breakthrough curve represents the relative contribution of the traced event to the recharge at the investigated soil depth [*Benettin et al*., 2015b] (Figure 2). To derive probability densities, the tracer mass breakthrough curves were normalized by the fraction of the precipitation that becomes recharge (Q/P). Q/P was calculated as the maximum of the cumulative tracer mass breakthrough curve of the recharge water (Figure 2). The medians of these event specific TTD of the recharge mass flux were computed for each rainy day (TT in Figure 2) for the investigated depths (TT_{10}, TT_{30}, MT_{50}, TT_{100}, TT_{150}, TT_{200}). The same procedure was applied for rainwater that leaves the soil profile by root water uptake, resulting in time variant median travel times of the water taken up by the roots in the unsaturated zone (RT in Figure 2).

In accordance to a concept proposed by *Heidbüchel et al*. [2012] for the catchment scale, the event specific TTD of the recharge water were multiplied by the recharge amount, superimposed, summed up, and divided by the total recharge to derive site specific master travel time distributions of the recharge water (MTTD). Here, we define recharge water as water that passes the −200 cm depth plane to ensure that the water will reach the groundwater and will not be used by the vegetation. The MTTD, which represent the average probability of a water particle to pass the soil at −200 cm depth at a certain time, were also computed for each meteorological season, to get the variation of the MTTD over the year. Of the MTTD, the median was calculated in accordance to the TT (Figure 2) to get a site specific representative median master travel time (MTT_{median}, Figure 2). Furthermore, the mean master travel time (MTT_{mean}) was calculated as the probability weighted average of travel time.

Additionally, the MTTD as a function of the cumulative flow since the input time was computed to assess flow corrected TTD. To do so, the event specific TTD of the recharge water were calculated as a function of the cumulative flow since the input and afterwards binned in 1 mm increments of the cumulative flow. For flow increments where more than one value of the event specific TTD was available, an arithmetic mean value was computed. For increments, where no value was available an interpolated value was computed. To study the influence of the meteorological forcing on the time variance of the TT, RT, and Q/P, we used the evapotranspiration sum of the 30 subsequent days after the corresponding rain event (ET_{30}) and the precipitation sum over the period of the TT_{200} (P_{TT}).

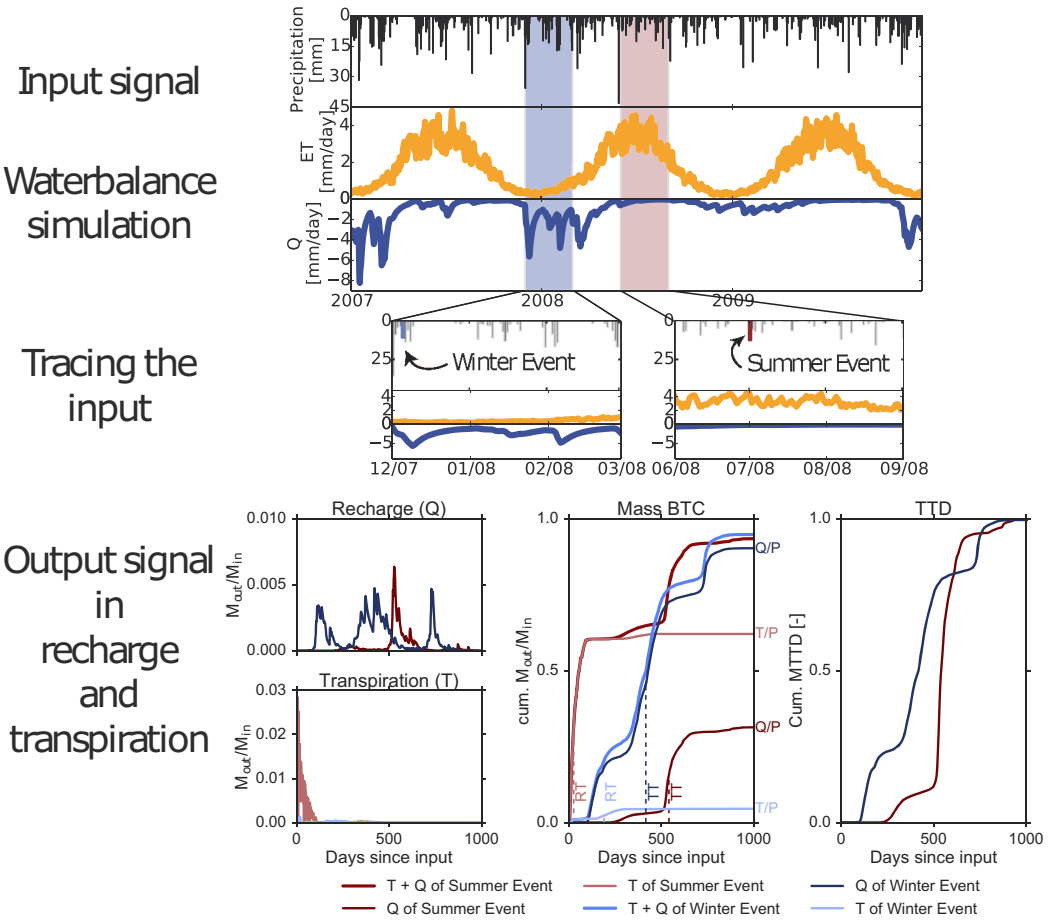

Figure 2. Conceptualization of travel time estimation with virtually tracing each precipitation input through the vadose zone. The concept is shown for two exemplary days: one in winter (5 December 2007) and one in summer (1 July 2008), with precipitation input of 10.6 and 9.9 mm, respectively. (bottom left) The output signals for the events are given as mass breakthrough curves (Mout/Min) for recharge at −200 cm depth (Q) and transpiration flux (T) individually. (bottom center) The cumulative mass breakthrough curves (Mass BTC) of the recharge and transpiration fluxes and the sum of both (T + Q) are shown for both events including the median travel times of the recharge (TT) and the transpiration (RT) and the fraction of recharge to evapotranspiration (Q/P). The travel time distributions (TTD) were derived by normalizing the mass BTCs of Q by the ratio Q/P.

2.5. Statistics

Statistical relations between two measures were generally tested by the Spearman's rank correlation and only for clearly linear relation the Pearson correlation was applied. A statistical significance of the differences between the data grouped over space (e.g., soil types) or time (e.g., meteorological seasons) was tested by the Kruskal-Wallis test. If the Kruskal-Wallis test resulted in statistical significant differences ($p < 0.05$), a posthoc test after Tukey and Kramer (Nemenyi) was applied to determine which groups differ significantly. Throughout the manuscript, we refer to the arithmetic mean when we use the term average.

3. Results

3.1. Site Specific Soil Hydraulic Properties

The site specific hydraulic properties derived by inverse modeling show some general patterns among the different soil types (Table 5). θ_s is on average 52 vol % and significantly higher in the top soil than in horizon 2 with 40 vol % and horizon 3 with 44 vol %. The values for θ_s are on average higher for the ST with 55, 45, and 44 vol % for the three horizons, than for the CM with 53, 38, and 43%, and for the AR with 51, 40, and 45 vol %. However, only for horizon 2, the θ_s is significantly higher for the ST than for the CM. In the third horizon, the differences between the three soil types with regard to θ_s are minor. The values for α of the topsoil are on average 0.038 cm^{-1} and significantly higher than in the horizon 2 and 3 ($\alpha = 0.014$ cm^{-1}).

Table 5. Overview of the Best Parameter Set and the Corresponding Model Efficiencies Regarding the Soil Moisture ($KGE_{\theta 10}$ and $KGE_{\theta 30+\theta 50}$), Isotope Profiles KGE_D and Resulting Multiobjective KGE_{mo} for Each Study Site and Averaged for Each Soil Type[a]

Site ID	θ_s1	$\alpha 1$	$n1$	K_s1	θ_s2	$\alpha 2$	$n2$	K_s2	θ_s3	K_s3	λ	$KGE_{\theta 10}$	$KGE_{\theta 30+\theta 50}$	KGE_D	KGE_{mo}
S_A	0.547	0.008	1.316	180	0.326	0.004	1.299	348	0.434	715	0.5	0.65	0.75	0.81	0.74
S_B	0.503	0.071	1.265	595	0.353	0.017	1.287	643	0.358	550	8.5	0.76	0.89	0.82	0.82
S_C	0.556	0.087	1.249	53	0.338	0.015	1.195	689	0.321	172	9.4	0.58	0.83	0.71	0.71
S_D	0.538	0.039	1.328	10	0.400	0.028	1.319	915	0.480	130	7.2	0.85	0.89	0.56	0.77
S_E	0.562	0.036	1.379	375	0.400	0.012	1.383	418	0.339	24	8.4	0.77	0.87	0.74	0.80
S_G	0.577	0.100	1.278	769	0.302	0.023	1.285	1000	0.437	373	6.3	0.76	0.81	0.67	0.75
S_H	0.520	0.071	1.296	646	0.419	0.006	1.584	853	0.495	233	5.3	0.59	0.86	0.74	0.73
S_I	0.569	0.003	1.526	580	0.409	0.010	1.221	1000	0.448	383	2.8	0.85	0.83	0.40	0.69
S_M	0.516	0.015	1.298	525	0.440	0.002	1.894	249	0.436	736	5.0	0.51	0.74	0.82	0.69
S_O	0.524	0.016	1.325	748	0.412	0.010	1.259	612	0.500	144	4.5	0.82	0.76	0.80	0.80
S_P	0.427	0.013	1.267	351	0.413	0.002	1.895	244	0.437	89	2.3	0.70	0.69	0.86	0.75
S_Q	0.543	0.021	1.314	278	0.478	0.010	1.382	501	0.479	469	10.5	0.78	0.86	0.57	0.73
S_S	0.477	0.048	1.270	931	0.300	0.016	1.229	872	0.409	150	27.3	0.75	0.85	0.82	0.81
S_T	0.470	0.012	1.374	1000	0.314	0.006	1.335	728	0.469	426	4.4	0.70	0.88	0.76	0.78
S_U	0.559	0.003	1.557	513	0.433	0.002	1.365	757	0.411	999	9.8	0.68	0.75	0.78	0.74
S_W	0.522	0.060	1.319	948	0.300	0.017	1.219	545	0.454	164	6.0	0.62	0.84	0.87	0.78
Sa_A	0.516	0.038	1.340	494	0.450	0.006	1.686	795	0.500	1000	12.7	0.82	0.93	0.87	0.87
Sa_B	0.469	0.043	1.187	439	0.417	0.017	1.170	848	0.373	627	12.4	0.79	0.91	0.88	0.86
Sa_C	0.596	0.075	1.235	585	0.382	0.003	1.425	617	0.445	931	6.9	0.75	0.86	0.78	0.80
Sa_D	0.456	0.030	1.298	632	0.404	0.009	1.325	812	0.496	1000	2.0	0.85	0.90	0.73	0.82
Sa_E	0.521	0.050	1.204	431	0.366	0.003	1.205	98	0.332	318	13.7	0.76	0.84	0.84	0.81
Sa_F	0.573	0.001	1.818	10	0.469	0.001	1.650	72	0.492	995	2.3	0.79	0.87	0.90	0.85
Sa_G	0.546	0.033	1.228	528	0.319	0.005	1.194	132	0.470	532	5.9	0.81	0.85	0.85	0.83
Sa_H	0.464	0.061	1.225	234	0.338	0.013	1.384	444	0.411	924	4.4	0.88	0.90	0.82	0.86
Sa_I	0.529	0.038	1.329	598	0.400	0.005	1.354	501	0.400	877	2.2	0.76	0.85	0.62	0.74
Sa_J	0.452	0.079	1.165	268	0.400	0.003	1.231	456	0.464	977	7.9	0.75	0.75	0.65	0.71
Sa_K	0.493	0.022	1.286	181	0.425	0.020	1.297	805	0.495	718	18.1	0.89	0.89	0.89	0.89
Sa_L	0.456	0.054	1.242	915	0.427	0.028	1.347	509	0.486	477	15.1	0.88	0.87	0.95	0.90
M_A	0.530	0.010	1.309	842	0.436	0.011	1.311	845	0.496	185	5.5	0.79	0.89	0.96	0.88
M_B	0.598	0.040	1.213	10	0.409	0.015	1.075	979	0.469	765	21.1	0.66	0.67	0.79	0.71
M_E	0.580	0.070	1.190	423	0.499	0.077	1.178	417	0.456	49	16.0	0.91	0.87	0.87	0.89
M_H	0.453	0.020	1.193	451	0.452	0.074	1.185	985	0.439	15	21.9	0.94	0.90	0.75	0.86
M_I	0.544	0.029	1.236	356	0.390	0.012	1.154	360	0.374	436	4.5	0.66	0.79	0.83	0.76
M_J	0.600	0.013	1.237	82	0.491	0.011	1.176	700	0.419	588	3.8	0.70	0.82	0.78	0.77
M_K	0.512	0.004	1.476	35	0.451	0.003	1.321	438	0.440	10	5.9	0.84	0.85	0.64	0.78
Cambisols	0.526	0.038	1.335	531	0.377[b]	0.011[b]	1.384	648	0.432	360[b]	7.4	0.71	0.82	0.73	0.754
Arenosols	0.506	0.044	1.296	443	0.400[b]	0.009[b]	1.356	507	0.447	781[a]	8.6	0.81	0.87	0.81	0.830
Stagnosols	0.545	0.027	1.265	314	0.447[a]	0.029[a]	1.200	675	0.442	293[b]	11.2	0.79	0.83	0.80	0.805
All study sites	0.523	0.038	1.308	458	0.399	0.014	1.338	605	0.439	491	8.6	0.76	0.84	0.78	0.791

[a]The superscripted letters for the average values of the soil types indicate significant differences.

The ST hold a special position, because they do not have lower values for α in the subsoil, leading to significantly higher α values in the subsoil compared to the CM and the AR. The values for n vary little within the range of 1.3 and 1.9 and do not show any significant differences between the horizons or the soil types. The hydraulic conductivity does not differ significantly among the horizons, but the ARs hold on average significantly higher K_s values (781 cm d^{-1}) in the horizon 3 than the CM (360 cm d^{-1}) and the ST (293 cm d^{-1}). The dispersivity ranges between 0.5 and 27 cm among the profiles and is on average higher in ST with 11.7 cm, than in the CM with 7.4 cm and the AR with 8.0 cm.

3.2. Fit Between Observed and Simulated Data

The soil moisture dynamics are generally well represented by the simulations (Figure 3), as indicated by the objective function values for the soil moisture in 10 cm that range between 0.51 and 0.94 and for the soil moisture in 30 and 50 cm which range between 0.67 and 0.93 (Table 5). The model efficiencies regarding the soil moisture are on average best for the AR soils. The mean of the objective function value for the soil moisture at 10 cm for the AR is 0.81 and significantly higher than for the CM (0.71), while the ST have on average similar values (0.79) compared to the AR. The temporal pattern in the observed soil moisture time series of high water contents during dormancy between October and May, followed by a drying up period leading to lowest water contents in July and August are well represented in the soil moisture simulations. While the differences between simulated and observed soil moisture at 10 cm is mostly within the accuracy of the soil moisture sensors (±3%), these differences are usually higher at 30 and 50 cm soil depth.

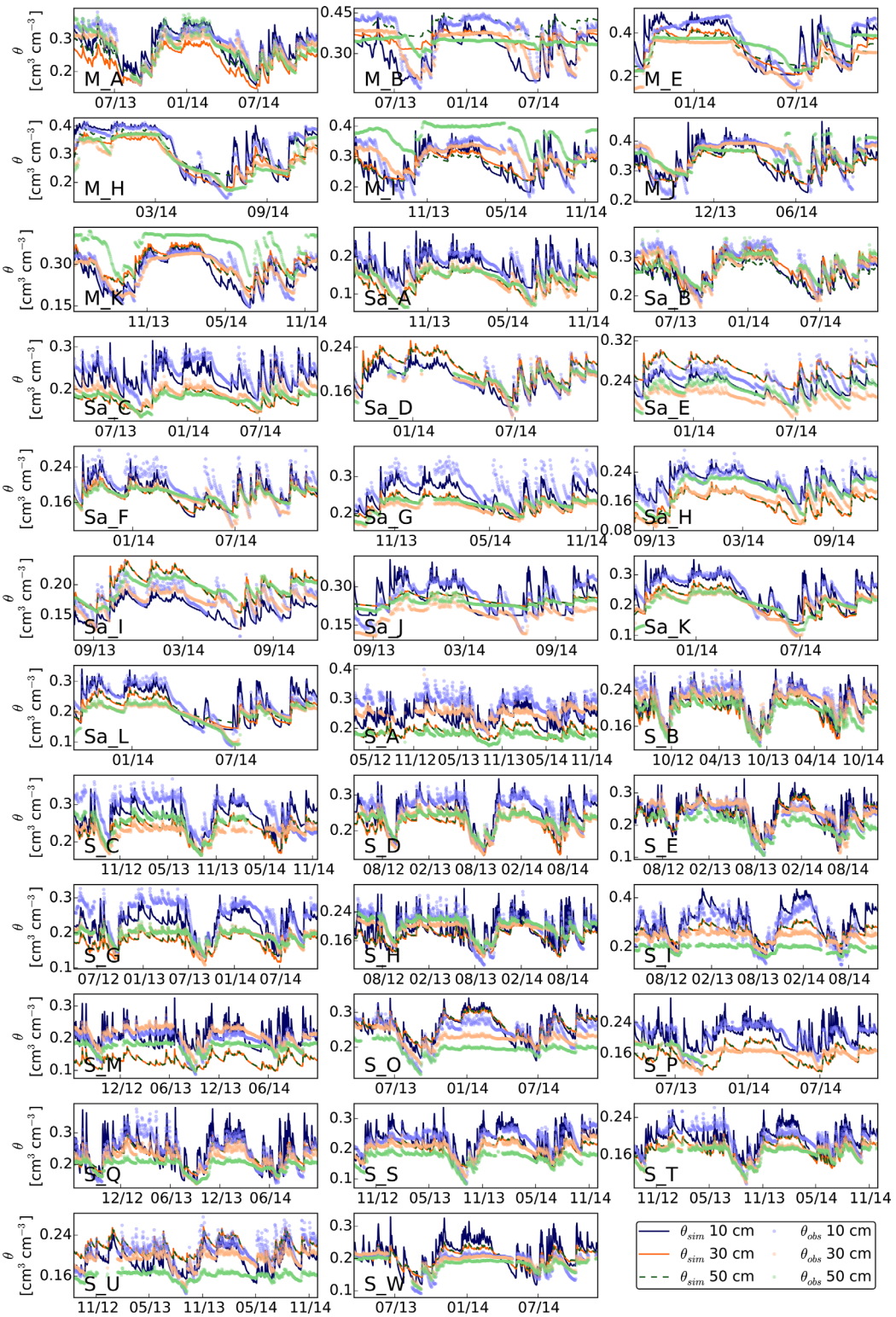

Figure 3. Observed and simulated soil moisture at each study site. Observed data were used for inverse modeling and the simulated data represent the best fit according to the multiobjective function KGEmo (equation (6)).

The simulations of the pore water isotopes reflect for most of the δ^2H profiles the pattern of the field observations (Figure 4). However, several sites, show for one of the profiles an offset in the simulations to either more enriched values (M_A, Sa_A, Sa_B, Sa_D, Sa_E, Sa_G, S_S) or more depleted values (M_E, Sa_J, S_G,

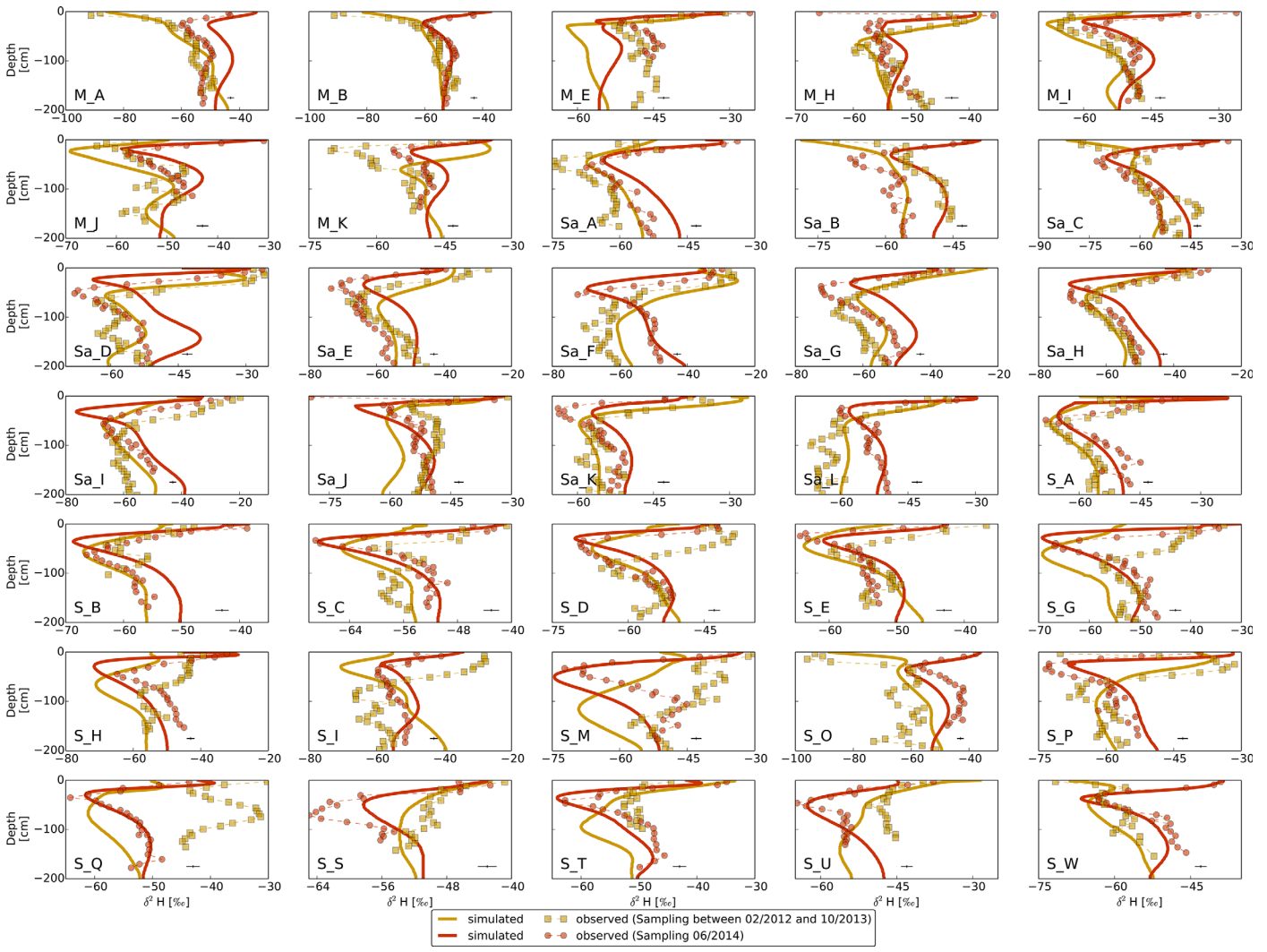

Figure 4. Observed and simulated δ2H profiles at each study site. Observed data were used for inverse modeling and the simulated data represent the best fit according to the multiobjective function KGEmo (equation (6)).

S_H, S_M). At a few sites also the shape of one of the δ^2H profiles is not well reflected (M_K, S_I, S_Q, S_T, S_U). The average model efficiency for the two δ^2H profiles at each site were generally higher for the ST and the AR with values for the objective function of 0.81 and 0.80 compared to the CM with 0.73. There is no significant correlation ($\rho = -0.28$) between the topographic slope at the study sites (Table 1) and the efficiency of the isotope profile simulation (Table 5). There is also no temporal pattern regarding the performance of the isotope profile simulations for the sampling period between February 2012 and October 2013. However, the simulations for the isotope profiles taken in June 2014 outperform the simulation of the previous pore water stable isotope sampling for more than two-thirds of the study sites. The overall performance for the isotope profiles lies between 0.69 and 0.90 and is on average 0.83 for the AR and 0.81 for ST, but lower for the CM with 0.75.

3.3. Travel Times Over Time

The travel time of water through the vadose zone is highly time variable. The median travel time of the recharge water (TT) for the period 2007–2010 varies at the individual study sites in the topsoil (TT_{10}) between 1 day and 100 days (Figure 5a). With depth the variation over time increases and the flashiness of the response decreases. At −200 cm depth, the variation of the TT_{200} at the individual sites reaches at least 300 days and up to 949 days (Figure 5f). The TT_{200} does not differ significantly among the meteorological seasons, with an arithmetic mean for TT_{200} over all study sites of 667 days for events during winter, 666

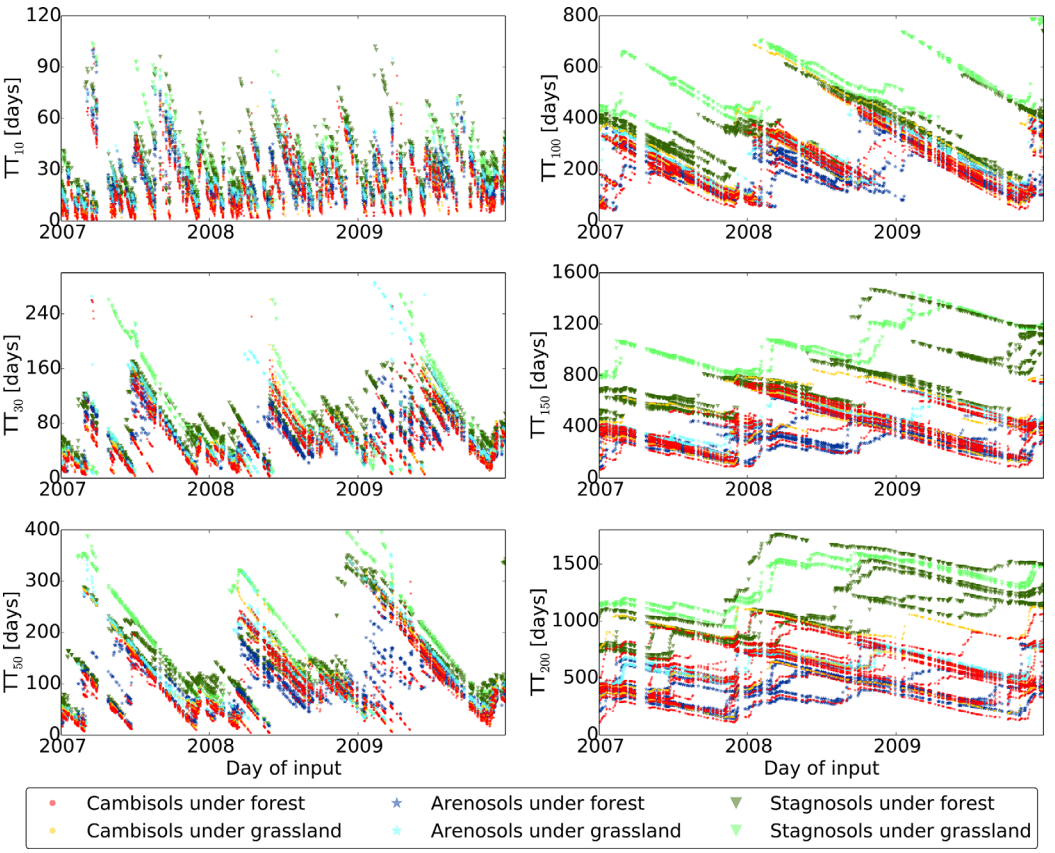

Figure 5. The time variant median travel times of the percolating water at −10 cm (a), −30 cm (b), −50 cm (c), −100 cm (d), −150 cm (e), −200 cm (f) for all 35 study sites with marker and color code according to the soil types and land use. Note the different scales of the y axes.

days for spring, 611 days for summer, and 607 days for fall. While the temporal dynamics of the median travel time at −10 cm depth are mainly driven by the precipitation events, between −30 and −100 cm, the median travel time shows in addition to the timing of rainfall a seasonal pattern with longer travel times for late winter and early spring.

In contrast, the median travel time of the transpired water (RT) is seasonally different, with significantly shorter RT for events during spring (41 days on average) and summer (30 days) compared to events during fall (133 days) and winter (136 days) (Figure 6a). The fraction of recharge of the precipitation (Q/P) differs significantly between seasons and is on average 0.41 for rain events during winter, 0.12 for events in spring, 0.26 for summer, and 0.53 for fall events (Figure 6b).

The MTTD show a seasonal pattern with peaks of high probabilities of recharge fluxes between 100 and 170 days, 370 and 470 days, 735 and 870, 1080 and 1200 (Figure 7). The medians of the MTTD (MTT_{median}) computed for the different seasons do not vary significantly over the year and are on average 569, 676, 604, and 553 days for the winter, spring, summer, and fall events, respectively (Table 6). However, the amount of the precipitation water that eventually becomes recharge, given as the Q/P in Figure 6d and the maximum cumulated MTTD for each season in Figure 8, is higher for the fall and winter events than for the spring and summer events. Neither the means of the MTTD (MTT_{mean}) nor the time averaged TT differ significantly from the MTT_{median} (Table 6) and correlate significantly ($\rho = 0.98$). The multimodal pattern of the MTTD is diminished for the flow corrected time and the shape approaches a pattern of a dispersion model (Figure 9). However, there are still peaks of higher recharge probabilities given for the flow corrected MTTD, but the seasonal signal is gone. The variability of TT is mainly driven by the subsequent precipitation amount following the precipitation events. There is a significant linear correlation ($r = 0.90$ on average) between the TT_{200} and the precipitation amount summed up over the estimated TT_{200}, defined as the subsequent rainfall index, P_{TT}. The slope of the regression between TT_{200} and P_{TT} is on average 0.62 with no significant

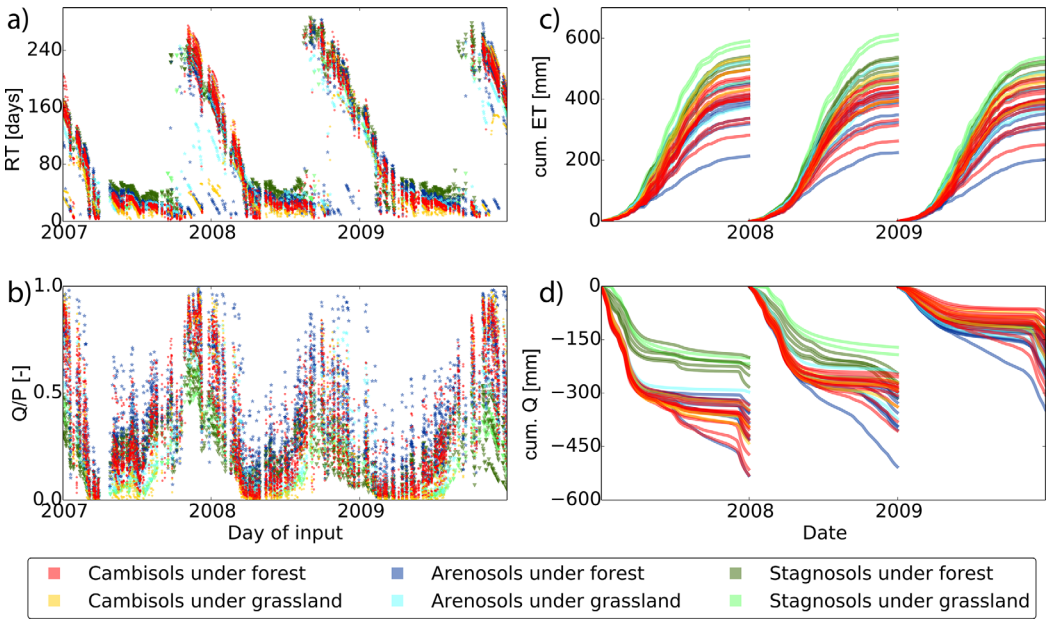

Figure 6. (a) The time variant median travel times of the transpired water RT, (b) the time variant recharge ratio Q/P, (c) cumulative evapotranspiration, and (d) cumulative recharge for all 35 study sites color coded according to the soil types and land use.

difference between the soil types. The antecedent precipitation prior to an event, the event size, or soil storage state during the event does not have an influence on the TT_{200} of the rainwater.

3.4. Travel Time Over Space

The differences of the TT among the studied soils are more pronounced with increasing soil depth (Figure 5). While the average TT_{10} for the ST is 31 days and thus, relatively similar to the CM with 17 days and AR with 24 days, the differences are more pronounced at −200 cm where TT_{200} for ST is with 1046 significantly longer than for the CM with 548 days and AR with 497 days (Table 6 and Figure 5f). Also, the average range of the TT_{200} for the period between 2007 and 2010 at the individual sites is on average 738 days for the ST and significantly higher than for the CM (560 days) and AR (496 days). However, the coefficient of variation of the TT_{200} is slightly lower for ST (0.20) than for CM and AR (both 0.25). The RT differs significantly between ST with on average 105 days and CM with 82 days or AR with 84 days (Table 6 and Figure 6a). Furthermore, a similar pattern is given for the average fraction between recharge and actual evapotranspiration in the MTTD (*Q*/*P*): the ST shows significantly lower *Q*/*P* of 0.31 compared to CM with 0.60 and AR with 0.55 (Table 6). This is even more pronounced for the fall and winter rainfall events (Figure 6b).

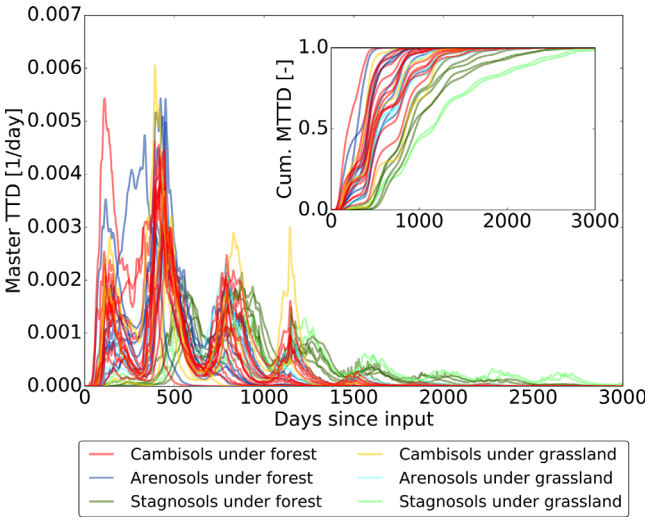

Figure 7. Master travel time distributions (MTTD) for the 35 study sites. Color code indicates the soil type and the land use. The inserted graph shows the Cumulative master travel time distributions (Cum. MTTD).

The MTTD for the different study sites show that the CM and AR hold similar seasonal patterns with peaks of high recharge probabilities starting at 40–100 days after the precipitation input, while for the ST, the event waters only contribute to recharge after 400 days after the rainfall (Figure 7). The MTT_{median} is almost twice as long for ST (958

Table 6. The Site Specific Data (Site ID) and Averaged Data for the Soil Types (Cambisols, Arenosols, Stagnosols) of the Meteorological Conditions in the Period Between 2007 and 2010 With Mean Annual Precipitation Sum (Precipitation), Average Air Temperature (T_{mean}), Potential Mean Annual Evapotranspiration Sum (PET), and Actual Recharge (Q)[a]

Site ID	Precipitation (mm)	T_{mean} (°C)	PET (mm y^{-1})	Q (mm y^{-1})	Average TT (days)	MMT_{mean} T (days)	MTT_{median} all events (days)	MTT_{median} Winter (days)	MTT_{median} Spring (days)	MTT_{median} Summer (days)	MTT_{median} Fall (days)	Average RT (days)	Average Q/P (–)
S_A	827	8.29	319	−327	384	374	389	388	372	330	400	79	0.66
S_B	827	7.78	380	−269	466	430	422	415	587	492	425	82	0.61
S_C	827	8.33	390	−278	523	485	446	432	605	520	441	90	0.56
S_D	827	8.27	425	−231	626	582	500	481	679	591	487	89	0.57
S_E	827	8.12	459	−187	667	600	507	485	689	593	492	88	0.48
S_G	827	8.09	400	−251	532	504	457	456	678	526	450	79	0.65
S_H	827	8.78	401	−267	421	398	413	410	421	341	419	82	0.68
S_I	827	8.56	493	−209	918	843	846	855	1026	905	831	85	0.62
S_M	827	8.19	307	−364	238	218	191	256	265	184	144	58	0.71
S_O	827	7.95	471	−222	840	773	863	873	962	876	848	96	0.48
S_P	827	8.43	399	−300	357	338	390	393	327	259	390	54	0.69
S_Q	827	8.34	461	−241	577	542	474	469	675	555	468	92	0.56
S_S	827	8.63	435	−203	584	594	473	452	674	565	468	100	0.45
S_T	827	7.97	375	−255	566	538	489	463	614	544	480	81	0.61
S_U	827	7.99	256	−386	361	365	363	361	331	325	391	75	0.68
S_W	827	8.66	420	−232	706	665	787	797	695	726	785	79	0.55
Sa_A	776	8.89	370	−241	319	329	342	367	342	258	234	85	0.54
Sa_B	776	8.63	424	−218	651	664	569	557	676	596	522	106	0.42
Sa_C	776	8.25	316	−313	398	411	412	399	375	448	431	83	0.58
Sa_D	776	8.35	383	−239	576	569	521	492	639	578	508	79	0.58
Sa_E	776	8.28	298	−322	480	504	463	434	546	523	463	97	0.57
Sa_F	776	7.97	200	−415	287	295	296	322	284	259	293	44	0.74
Sa_G	776	8.09	362	−274	610	617	568	529	647	588	529	89	0.51
Sa_H	776	8.61	388	−258	418	415	428	414	409	496	443	86	0.58
Sa_I	776	8.72	351	−310	401	407	416	402	377	475	433	81	0.57
Sa_J	776	8.80	355	−299	585	616	564	591	679	586	530	68	0.63
Sa_K	776	8.80	487	−174	647	645	520	488	696	592	512	100	0.36
Sa_L	776	8.95	434	−222	590	614	505	485	702	587	507	85	0.52
M_A	790	9.49	496	−151	1026	915	837	822	986	897	830	101	0.36
M_B	790	9.36	413	−217	963	1027	907	836	1033	935	853	116	0.36
M_E	790	10.02	514	−144	1246	1240	1161	1158	1428	1264	1114	95	0.28
M_H	790	9.21	529	−126	1208	1251	1120	1150	1347	1087	1027	100	0.18
M_I	790	9.48	469	−185	901	859	832	797	879	869	842	101	0.38
M_J	790	9.60	447	−167	1031	952	892	840	985	925	865	112	0.33
M_K	790	9.40	485	−131	1238	1077	959	994	1044	970	912	112	0.29
Cambisols	827	8.27[b]	399[b]	−263[b]	548[b]	516[b]	483[b]	490[b]	599[b]	514[b]	470[b]	82[b]	0.60[b]
Arenosols	776	8.53[b]	364[b]	−274[b]	497[b]	507[b]	467[b]	456[b]	531[b]	498[b]	450[b]	84[b]	0.55[b]
Stagnosols	790	9.51[a]	479[a]	−160[a]	1088[a]	1046[a]	958[a]	942[a]	1100[a]	992[a]	920[a]	105[a]	0.31[a]
All	798	8.6	403	−246	638	619	572	569	676	604	553	87	0.52

[a]Furthermore, the arithmetic mean of the time variant median travel time of the recharge (Average TT), the mean master travel times of the recharge (MTT_{mean}), the median master travel times of the recharge (MTT_{median}) for all events and for the different seasons and the arithmetic mean of the time variant median travel time of the transpiration water (Average RT) and the recharge-evapotranspiration fraction (Q/P) are listed. The superscripted letters for the average values of the soil types indicate significant differences.

days) than for CM (483 days) and AR (467 days) (Table 6). The significant longer MTT_{median} for the ST are persistent over the year and the CM and AR show for all seasons shorter MTT_{median} (Figure 8).

The small differences of the MTTD between forested or grassland sites indicate that land use has only a minor influence on travel times. Grassland sites tend to have lower recharge amounts than forested sites, but differences are not significant (Figure 7). The time averaged TT_{200} correlates significantly with the arithmetic mean of the time averaged actual evapotranspiration (AET) amount ($\rho = 0.84$). Accordingly, there is a significant negative correlation between the TT and the average recharge amount ($\rho = -0.89$). The average summer temperature is significantly higher for the ST with 16.1°C than for the CM (14.9°C) and the AR (15.1°C), resulting in significantly higher annual ET sums for ST with 479 mm compared to CM with 399 mm and AR with 364 mm (Table 6 and Figure 6c). Also regarding the recharge amounts, the ST hold a special position, since their average annual recharge is with 160 mm significant lower than for CM with 263 mm and AR with 274 mm (Table 6 and Figure 6d).

Differences with regard to the topography were only tested for the CM and AR, since none of the study sites of ST are defined as hillslopes. Plateau sites were found to have on average longer MTT_{median} (547 days)

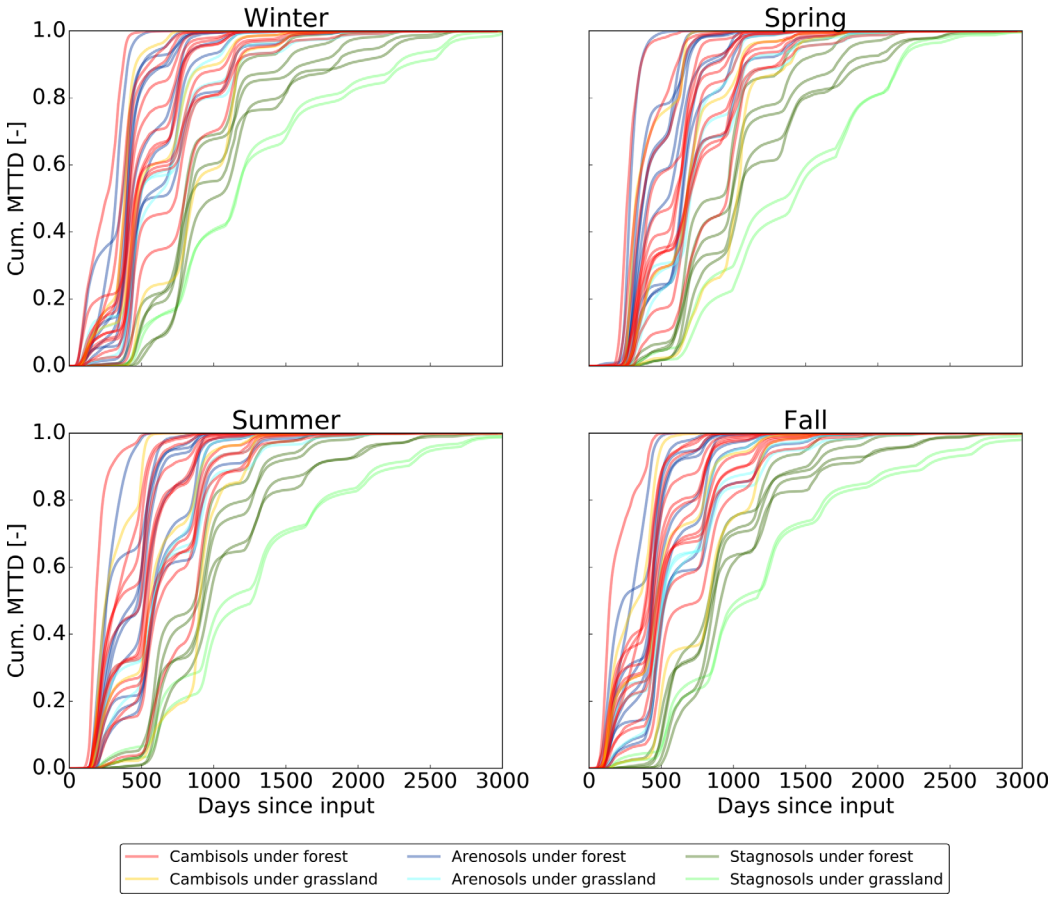

Figure 8. The site specific cumulative master travel time distribution (Cum. MTTD) computed for each season.

than the hillslope (454 days) and footslope sites (470 days). However, the differences are not statistically significant. A possible influence of the aspect for the forested hillslope sites of the CM and AR was also tested. North facing slopes of these two soil types have on average a longer MTT_{median} (489 days) than south facing hillslopes (413 days), but again, the differences are not statistically significant.

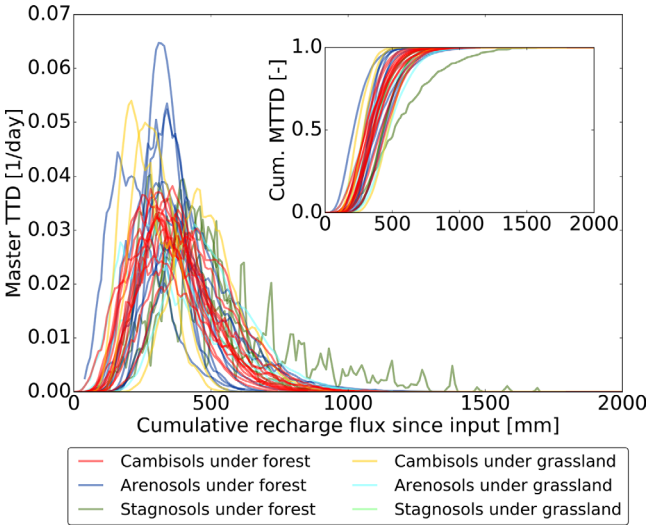

Figure 9. Master transit time distribution as a function of the cumulative recharge flux since the input. The inserted graph shows the cumulative master travel time distributions (Cum. MTTD). Color code indicates the soil type and the land use.

4. Discussion

4.1. Site Specific Soil Hydraulic Parameters

Similar to our findings of elevated θ_s-values in clayey soils, also look up tables [e.g., *Wessolek et al.*, 2009] and pedotransfer functions [e.g., *Schaap et al.*, 2001] report higher θ_s with increasing clay contents. Also regarding the α and n values, the inverse modeling results are in line with look up tables that show higher values for coarser material [*Wessolek et al.*, 2009]. The inversely estimated K_s are on average in the upper range of the listed values [*Wessolek et al.*, 2009], which

might be caused by the compensation of the lack of bypass flow in the model, resulting in K_s from inversion being an effective parameter. The inversely determined K_s values are within the wide range of laboratory measurements (using the KSAT UMS, Munich, Germany) on 88 soil cores taken mainly in the upper 20 cm of soil. Also the other parameters (θ_s, α, and n) derived by inverse modeling are within the range of laboratory results (derived with the UMS Hyprop device, Munich, Germany), except for three AR sites that hold higher n and four sites of AR and two sites of ST that hold higher α values. Therefore, our inverse model procedure resulted in realistic parameter sets, representing textural dependencies that have been reported by others. In contrast to pedotransfer functions, the applied calibration procedure made it possible to derive site specific water flow and solute transport parameters. Compared to laboratory measurements on soil cores, the inversely determined parameter sets are an effective representation of the prevailing hydraulic characteristics on the scale of the model application and should therefore be more realistic for the application in the soil profile [see also *Sprenger et al*., 2015b].

4.2. Fit Between Observed and Simulated Data

The high model efficiencies for the soil moisture simulation at 10 cm depth show that the weighting of the objective function was effective in achieving a good representation of the soil moisture dynamics in the topsoil, which is crucial for an appropriate representation of the actual evapotranspiration. The higher deviations between observed and simulated soil moisture data at 30 and 50 cm can be explained by the arrangement of the soil profile into discrete horizons that are represented by different soil hydraulic properties in the model. In reality, soils are highly heterogeneous and horizons often hold gradual textural changes, instead of sharp boundaries. Such discrepancy between model setup and field conditions can lead to responses at 30 and 50 cm that are not well represented in the simulations (e.g., M_I, M_K, Sa_E, Sa_H, S_A, S_I, S_M, S_U in Figure 3). Consequently, the performance of the soil moisture simulations was better for the relatively uniform sandy AR than for the structured CM.

Since there is no relation between model performance regarding the isotope profile simulations and the slope of the sites, the influence of lateral flows does not or just slightly shape the pattern of the pore water stable isotope profiles in the top 1.5–2 m. A similar dominance of vertical flow processes was also found in pore water isotope studies at steep hillslopes in the Tanakami Mountains of Japan [*Asano et al*., 2002] and in the Swiss Alps [*Mueller et al*., 2014]. However, lateral flows were shown to have an influence on the pore water composition in glacier tills during snow-melt [*Stumpp and Hendry*, 2012]. Even though the CM on the hillslopes in our study hold in the B-horizon horizontally aligned slate fragments in a periglacial slope deposit, a systematic shift of the simulated compared to the observed isotope profiles cannot be observed. However, at the sites S_I, S_O, and S_P (sampled in March after or during snowmelt) peaks of isotopically depleted pore waters in depth below 100 cm were not represented in the simulation indicating possible influences of lateral flows. Nevertheless, several other isotope profiles taken during or after snowmelt do not show such a isotopic depletion at a certain depth as observed for example by *Stumpp and Hendry* [2012] and *Peralta-Tapia et al*. [2014]. The simulation of the isotope profiles taken on south facing hillslopes in the schist area shows an isotopic depletion compared to the observation for the sampling campaigns in 2012 and 2013 (e.g., S_G, S_H, S_M, S_Q, and S_T in Figure 4). Such a discrepancy of isotopically enriched observations compared to the simulations can result from a locally altered isotopic signal in the infiltrating input water due to isotopic enrichment as a result of evaporation from the interception storage in the canopy or litter [*Allen et al*., 2014; *Brodersen et al*., 2000] or removing water from the beginning of the precipitation event. The north facing study sites where evaporation fractionation of the isotopic input signal is expected to be smaller than on the south facing slopes do not show such an offset. Thus, an implementation of the evaporation fractionation effects into the interception module would possibly improve the model accuracy. Some isotope profiles from the sampling campaign in June 2014 show isotopically depleted values compared to the simulations (M_A, Sa_A, Sa_B, Sa_D, Sa_E, Sa_G, Sa_H, and S_S in Figure 4). Such an offset toward isotopic enriched vales for the simulations is possibly due to an inaccurate representation of the root water uptake, which might overestimate transpired water in the spring time, leading to an intense loss of pore waters during a time were the pore water in the topsoil is dominated by depleted winter rainwater. However, these deviations between simulated and observed isotope profiles do not show a pattern regarding the sampling time, indicating that the simulations are not generally missing major processes (e.g., snowmelt, seasonal root water uptake). Similar to the soil moisture simulations, also for the isotope profile simulations, the model efficiency for the CM was lower than for the AR and ST. Thus, the

assumptions of the Richards equation and the advection-dispersion equation to simulate the subsurface processes cause more difficulties in the CM that have high rock contents and structured soils than for the more homogenous soils of the AR and ST.

Neglecting the upper 15 cm of the pore water stable isotopes for the inverse modeling procedure was shown to (i) minimize the effect of possible isotopic enrichment via soil evaporation that is not accounted for in the model code, (ii) exclude possible effects on the pore water isotope laboratory analysis due to high organic matter contents in the Ah-horizon, and (iii) minimize the effect on the objective function by an event based pore water isotopic signal in the topsoil, which holds far less information about the dispersivity processes than the pore waters below 15 cm soil depth. Thus, the lacking representation of the evaporation enrichment of the pore waters in the HYDRUS code is of minor influence on the model performance, although an isotopic fractionation signal (higher d-excess) was found in several isotope profiles in the upper 20 cm. The pore water stable isotope data gathered in the field below 20 cm, lysimeter studies (e.g., *Stumpp et al*. [2012] and *Maloszewski et al*. [2006]), and a global comparison between groundwater and rainwater isotope data [*Jasechko et al*., 2014] have shown that the recharge water and groundwater in the temperate climate show no isotopic enrichment. Thus, isotopically enriched pore waters in the topsoil are of minor relevance due to their small contribution to the recharge flux and due to the mixing that diminishes the evaporation fractionation signal during the percolation through the soil.

4.3. Mean Master Travel Times

The average median travel time in the upper 50 cm (TT_{10}, TT_{30}, TT_{50}) are in the same magnitude as mean travel times estimated with lumped approaches for these depths in other studies [*Asano et al*., 2002; *Kabeya et al*., 2007, 2011; *Kim and Jung*, 2014; *Kudo et al*., 2013; *Muñoz-Villers and McDonnell*, 2012; *Timbe et al*., 2014]. However, with increasing depth, some of our results for the average TT_{100} and TT_{150} are longer than mean travel times reported in other studies for these depths [*Kabeya et al*., 2007, 2011; *Muñoz-Villers and McDonnell*, 2012]. The mean master travel time (MTT_{mean}) estimated for the depth of −200 cm is at several sites of CM and AR (43%) within the range of 302–509 days reported by *Kabeya et al*. [2011] for the master travel time in 200 cm soil depth for the freely draining forested Cambisols on heavily weathered gneiss. Our travel time derived for soils in the field are mostly higher than the results of travel time modeling for the outflow of lysimeters. *Stumpp et al*. [2009] found for a lysimeter filled with a Regosol taken in the field mean travel times of 315–380 days under similar precipitation sums than at our study sites. The relatively short travel times in the lysimeter study are likely caused by the sandy gravels that followed a silty A-horizon in the Regosol, since the gravel size highly impacts the travel times in lysimeter studies [*Maloszewski et al*., 2006]. Since lumped transport models generally assume time invariance, their results are limited to mean travel times integrated over a certain time period, instead of variable mean travel times as calculated in our soil physical simulations.

However, the information content of mean travel time is limited, since it neglects the spatiotemporal spreading of the tracer [*McDonnell et al*., 2010] and is likely to be underestimated due to effects of aggregation of flow paths, as shown for catchments by *Kirchner* [2016b]. Instead, TTD account for the heterogeneity of water flow processes within a system due to a consideration of the shape and the tails [*Godsey et al*., 2010]. A possible underestimation of the tails of TTD can have a strong effect on mean travel time estimates, even when the simulated stable water isotopes data show a good agreement to the measured data [*Seeger and Weiler*, 2014]. The multimodal nature of the MTTD in our results further questions the meaning of the mean travel time for the vadose zone, since it does not account for the very dynamic system behavior.

4.4. Time Variance of the Median Recharge Travel Times

While the widely used lumped model approaches do not take variable travel times into consideration, our soil physical simulations enable us to assess the variation of the median recharge travel times (TT). The simulations further question the application of mean travel times in a highly dynamical system like the unsaturated zone. The flashy variation of the TT in the topsoil is due to the year-round frequent precipitation (Figures 5a and 5b). Over the soil depth, the flashiness dampens and the long term precipitation patterns become the driving factor of the time variance of the TT (Figures 5c–5f).

The relatively rapid increase of the TT in our simulations within the upper 50 cm is due to a strong dampening of the isotopic fluctuations of the precipitation within the upper 50 cm as was also found in several

previous pore water isotope studies [*Asano et al*., 2002; *Bertrand et al*., 2014; *Kudo et al*., 2013; *Muñoz-Villers and McDonnell*, 2012; *Timbe et al*., 2014; *Wang et al*., 2010]. The flashy behavior in the topsoil and the decrease of flashiness with depth is in line with other studies based on either soil moisture or lysimeter data [*Kim*, 2014, *Lindström and Rodhe*, 1992; *Queloz*, 2015a].

A similar relation between TT and subsequent rainfall amount as we found for the pedon scale was also reported for the hillslope scale by *McGuire et al*. [2007]. They reported a correlation coefficient of 0.81 between TT (e.g., "50% mass recovery") and the 30 day subsequent rainfall amount, based on breakthrough curves of virtual tracer injections at different times of the year leading to nonsteady TTDs. *Rinaldo et al*. [2011] underlined the time variable character of mean travel times of flows at the hillslope scale with theoretical numerical simulations. Our finding that rainfall is the main driver for the mean travel time in the soil profiles is in line with results for the catchment scale, where a correlation between mean travel times and both precipitation amount [*Hrachowitz et al*., 2009a,b] and intensity [*Hrachowitz et al*., 2010] for several headwater catchments in the Scottish Highlands were reported. Furthermore, precipitation driven (flashy) variable TT were presented by *Sayama and McDonnell* [2009] with a distributed rainfall-runoff model and by *van der Velde et al*. [2015] with conceptual models of different mixing assumptions. *Heidbüchel et al*. [2013] emphasized in their study on two subhumid catchments that the precipitation pattern, rather than simply the precipitation amount, is a dominant control of mean travel times. Hence, the relation between precipitation and travel times that we could observe at the pedon scale seems to be true also for the hillslope and catchment scale.

4.5. The Shape of the TTD

The multimodal shape of the MTTD derived from the soil physical modeling in our study clearly shows the high influence of evapotranspiration on the recharge probabilities in temperate climates. Such dynamics are not considered in travel time estimations with the usual lumped convolution approaches that assume unimodal distributions [e.g., dispersion-distributions, gamma-distributions, exponential-distributions, *McGuire and McDonnell*, 2006, 2010]. The vadose zone TTDs found at our field sites do not show such a smooth distribution, but rather peaks of higher probabilities during seasonally high recharge periods. Such "multimodal and complicated responses" were also derived for "hydrometric TT" based on soil moisture time series by *Kim and Jung* [2014]. While our MTTDs derived for each season do not show pronounced differences in MTT_{median} or skewness, in a monsoon climate, the TTDs of the rainy season showed higher skewness and kurtosis towards shorter travel times compared to TTDs of spring and fall [*Kim and Jung*, 2014]. *Kim and Jung* [2014] concluded that the intermittent rainfall was governing the multimodal TTDs for the upper 60 cm of the vadose zone. Since precipitation is more evenly distributed in Central Europe, the seasonality in recharge fluxes is induced by seasonally variable ET in our study. We see therefore in our MTTD earlier and higher peaks for rainwater introduced during winter or fall (Figure 8). The central role of the climatic forcing for the nonstationary behavior of the recharge TTD that we see in our simulations, was also shown by a lysimeter experiment of *Queloz et al*. [2015a], where several rainfall events were spiked with different fluorobenzoates. *Queloz et al*. [2015a] showed partly overlaying flow corrected breakthrough curves of injections close in time, which is in line with our simulation results (data not shown). Due to the limited tracer injections, *Queloz et al*. [2015a] could not apply the concept of MTTD. However, our results show that MTTD can be derived from flow corrected data, suggesting that the spectrum of the TTD results from an interplay between ET rates, precipitation frequency, recharge, and dispersion processes in the vadose zone.

Similar to the nonsteady TTDs on the pedon scale, also at the hillslope, physically based model simulations showed that TTDs are largely controlled by storm events with little to no tracer breakthrough during summer periods and a remobilization of the tracer after the system was wetted up again [*Ali et al*., 2014; *McGuire et al*., 2007; *Rinaldo et al*., 2011; *Weiler and McDonnell*, 2007]. If ET is not taken into account, the TTD has a left skewed shape and loses its seasonal variability with peaks of high recharge probabilities during fall and winter [*Ali et al*., 2014]. Such conditions with higher recharge rates during winter are generally found in temperate regions, as shown via ratios of the isotopic composition in the precipitation and groundwater by [*Jasechko et al*., 2014]. At the catchment scale, the shapes of TTDs were found to be driven by rainfall and dry periods [*van der Velde et al*., 2010] or wetness state [*Hrachowitz et al*., 2013] based on numerical flux tracking. However, a seasonal pattern of the TTD with higher recharge probabilities during fall and winter as found for the point and hillslope scale has not been reported for the catchment scale. Due to the spatially distributed input and the various flow paths and flow path lengths [*Kirchner et al*., 2001] and the mixing of the water [*Benettin et al*., 2013a], the seasonal signal of the vadose zone TTD is likely to

disappear for the TTD of the catchment outlet [*Kirchner*, 2016a, 2016b]. For example, the catchment of the Huewelerbach, in which the AR are located, shows very little variability of the base flow, due the big groundwater reservoir in the sandstone [*Wrede et al*., 2015]. Under such conditions, seasonal pulses of the vadose zone recharge (and its isotopic composition) will be damped and not seen in the stream. On the other hand, for the Weierbach with its CM soils, the groundwater storage is smaller and the discharge shows a seasonal pattern with regard to base flow and event responses [*Wrede et al*., 2015]. Here, the TTDs of the CM can partly explain the processes on the catchment scale. At the Wollefsbach (ST soils), a flashy response to rainfall is observed especially during wet periods [*Wrede et al*., 2015], which shows that near stream processes, possibly overland flow and artificial drainage systems are important for discharge generation. Thus, the long travel times and variable TTD of the ST will only influence the tail of the catchment TTD for the Wollefsbach. In general, our results for the TTDs through the upper 200 cm of the vadose zone might partly explain the long tails that were observed for catchment TTDs [e.g., *Godsey et al*., 2010; *Hrachowitz et al*., 2013; *Kirchner et al*., 2010].

4.6. Time Variance of the Transpiration Travel Times

While most travel time studies limit their surveys to the recharge (e.g., at defined soil depth) as solely considered outflow, we expanded the travel time concept to the sink within the soil via root water uptake. Our findings highlight the importance of root water uptake dynamics on vadose zone processes and provide information on the length of time it takes for soil water to be taken up by roots, including its temporal variability (RT).

We found that the variation of the RT is mainly driven by the seasonal variability of the ET (Figure 10). If the subsequent ET sum after a rain event (ET_{30}) is $>$70 mm, the RT is usually $<$50 days. A ET_{30} of $>$70 mm is almost always the case for the summer events and for most of the spring and some fall events. During the transition from winter to spring, the RT gradually gets shorter. Sometime in fall, just before the defoliation, the RT abruptly switches from short times to the longest times (Figures 6a and 10). The winter precipitation events result in intermediate RT ranging between the late fall events and the early spring events. While such a seasonal pattern cannot be seen in the 4 months of the simulations of the evapotranspiration travel times by *Queloz et al*. [2015b] for their lysimeter study, *Harman* [2015] showed for the catchment scale the variation of the travel times of the evapotranspired water. This analysis showed that older ($>$40 days) water is more likely to be evapotranspired during summer, while the ET during winter is mainly limited to younger water ($<$40 days) [*Harman*, 2015]. Our simulations of the RT are in line with the simulations by *Harman* [2015] for the age distribution of ET water, since the high transpiration rates in spring and summer and short RT for spring and summer events will result in increased root water uptake of old water (rainwater from fall and winter).

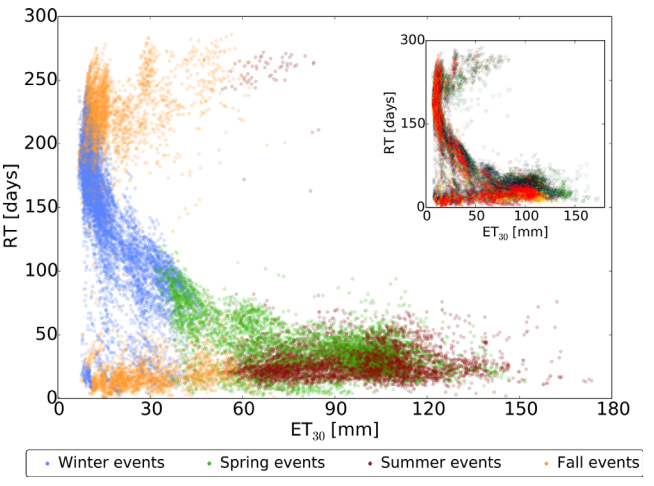

Figure 10. The median travel time of transpired water (RT) as a function of the ET sum of the subsequent 30 days after the corresponding event (ET30). Color code according to the timing of the precipitation input. The inserted graph shows the same data, color coded according to the soil types and land use (color code as in Figure 5).

Our simulations show that the interplay between the seasonality of recharge and transpiration leads to a pronounced variability of the ratio between recharge and ET. This variation can be partly explained by the ET_{30} leading to an anticlockwise hysteresis as shown in Figure 11. Precipitation events in spring are most likely to end up being transpired during the summer when ET is high, while some water of the summer rain will pass the root zone during the subsequent fall and winter. Precipitation events after the defoliation in fall are very likely to become recharge, since most of the rainwater will travel through the root zone during low ET rates of the following winter. The winter precipitation can leave the soil either via recharge

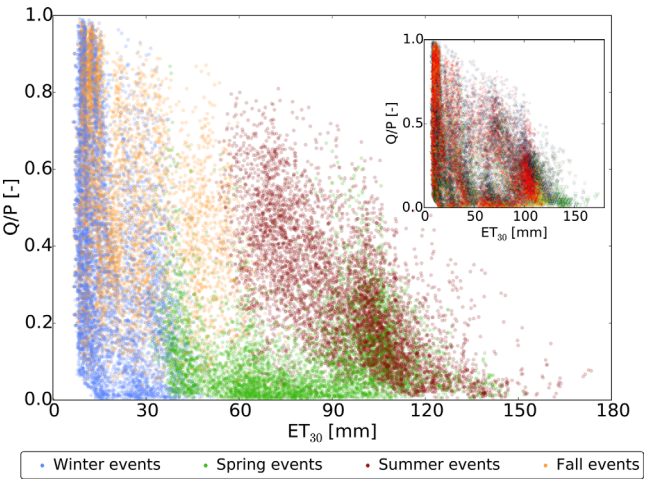

Figure 11. Relation between the recharge-evapotranspiration fraction (Q/P) of the event water and the ET sum of the subsequent 30 days (ET30). Color code according to the timing of the precipitation input. The inserted graph shows the same data, color coded according to the soil types and land use (color code as in Figure 5).

or ET, mainly depending on the timing of the rain event. Thus, our findings are in line with *Queloz et al.* [2015b], who also found in their lysimeter study a seasonality in *Q/P* with a higher share of precipitation becoming recharged in late fall and early winter compared to late summer or early fall.

Our findings of a time variable *Q/P* relation on the pedon scale are only partly seen on the bigger scale. The catchment that consists mainly of Cambisols (Weierbach) and Stagnosols (Wollefsbach) show seasonality in the *Q/P* in the stream flow data [*Wrede et al.*, 2015], but the catchment dominated by Arenosols (Huewelerbach) does not show such a variability due to the groundwater dominated flow regime [*Wrede et al.*, 2015]. Thus, the hydrologic dynamics in the vadose zone play a minor role for the discharge processes due to the large storage volume in the vadose zone and the groundwater reservoir in the sandstone of the Huewelerbach. As a consequence, the information given in the stream data to answer hydrological processes in the soil vegetation interaction is limited.

The importance of the vegetation dynamics on the vadose zone encourages the use of ideal tracers such as water stable isotopes. Water isotopes can be taken up by plants as part of the water molecule and thus transpiration only alters soil water content but not the pore water stable isotopic composition. Therefore, pore water stable isotope data is more suitable for the investigation of transpiration losses than an artificial conservative tracer.

4.7. Spatial Variability of Travel Times

The travel times of our study sites are mainly governed by the soil texture that developed on the different geological settings, while the differences due to land use, topographical position, and aspect are of minor importance. Given the possibly pronounced variation depending on the prevailing soil type and geology as shown in the significant differences between ST and both CM and AR in our study, the soil textural or geological information seem to be crucial for travel time studies. The influence of vegetation and accompanied biological activity on soil structure is likely to be underrepresented in our simulation, since their impact on preferential flow paths is not explicitly accounted for in our modeling approach. Further, the relatively simple representation of the rooting systems might as well limit the explanatory power of our simulations. However, the stronger influence of soil type compared to vegetation effects was also seen in the pore water stable isotope dynamics reported for soils in the Scottish Highlands [*Geris et al.*, 2014]. Thus, soil types need to be accounted for when comparing different study sites. Our simulations reveal that, even within one soil type, the travel time can vary intensely due to the strong heterogeneity in the subsurface. The high spatial variation of vadose zone travel times is supported by *Kabeya et al.* [2011], whose study was limited to four sites located within 50 m distance, but still, the mean travel times in 200 cm soil depth varied considerably among the sites. Most of the vadose zone travel time studies are limited to few study sites and a spatial coverage and sample size as presented in our study is unique. The focus in previous studies is often on differences of the vadose zone travel times at various depths at one site [*Lee et al.*, 2007] or few sites of different topographies [*Asano et al.*, 2002; *Kabeya et al.*, 2007, 2011; *Kim*, 2014; *McGuire and McDonnell*, 2010; *Muñoz-Villers and McDonnell*, 2012; *Stewart and McDonnell*, 1991] and/or land uses [*Kudo et al.*, 2013; *Timbe et al.*, 2014]. These listed studies are usually limited to the upper 40 to 100 cm soil depth, because they use wick samplers and suction lysimeters that are usually limited to the upper 100 cm. In contrast, our methodology of pore water sampling and travel time estimation allows us to consider also deeper soil depths or even including the geological setting, while keeping labor and time comparably low.

Studies which compared the travel times at sites of different topographical positions saw generally a dominance of vertical flow even at hillslopes [*Asano et al*., 2002; *McGuire and McDonnell*, 2010; *Muñoz-Villers and McDonnell*, 2012; *Timbe et al*., 2014], which supports our 1-D model approach. Closer to the drainage system the influence of lateral flow paths increases as seen in both simulated travel times [*Kim*, 2014; *Kim and Jung*, 2014] and observed pore water stable isotopes [*Garvelmann et al*., 2012]. Such effects have been neglected in our study, since areas of possible groundwater influence were excluded. Vertical bypass during high intensity rainfall [*Weiler and Naef*, 2003] was not taken in to account for our simulations. Even though the applied Richards equation does not consider bypass flow, the inverse modeling approach allows us to derive effective soil hydraulic parameters to simulate the water flow and tracer transport processes. Furthermore, as intense rainfall is relatively rare, 90% of all the rainy days in the simulated period had less than 11.5 mm d^{-1} of precipitation and about 80% of the amount of precipitation input enters the soil on rainy days of less than 20 mm, preferential flow is less likely and less intense (see also review by *Nimmo* [2007]).

5. Conclusions

The unique experimental setup of site specific pore water stable isotope profiles, soil moisture time series, air temperature, solar radiation, and LAI measurements allowed us to virtually track the transient water flow and transport through the upper vadose zone at 35 sites by using a soil physical model. This model was calibrated both to soil water dynamics and deuterium profiles. The resulting data set of transit times in the unsaturated zone was then analyzed for spatial and temporal variability. The time rainwater needs to travel until it is either taken up by plants or has reached a certain depth in the soil is highly variable. While the time-variance of median transit time of recharge is mainly driven by the subsequent rainfall amount, the dynamic pattern of the median transit time of transpired water is governed by the seasonal ET. The recharge travel time varies over time, with flashy responses in topsoil according to the rainfall pattern, seasonal influences between −30 and −100 cm depth, and a much dampened variation at −150 and −200 cm depth, following the long term rainfall pattern. The transpiration travel time has a pronounced seasonal variation and also the *Q*/*P* ratio shows an annual cycle driven by meteorological conditions (evaporative atmospheric demand and seasonally active vegetation). This time-variable climatic forcing is also signaled in the multimodal nature of recharge probabilities in the MTTD. We thus conclude regarding our first research question that the applied soil physical simulations were successful in deriving time variable travel times and explaining the variability by the environmental drivers.

Regarding our second research question, our survey demonstrated the potential to study the travel time variability in space. However, the local heterogeneity of the soil hydraulic characteristics does not allow for simplified conclusions regarding spatial organization of vadose zone travel times across the catchment to identify controls such as land use, topographical position, or aspect. The spatial variability of the hydrologic response is mainly influenced by soil texture and structure on the different soil types developed on different geologies. Thus, differences between the investigated soil profiles across the catchment are mostly driven by soil types. Although the presented travel times for the study sites are in accordance with the general conceptual representation of the vadose zone processes in the three geological regions, TTD at the catchment outlets are likely to differ, especially if a large groundwater storage is present. Such differences between pedon and catchment scale are due to the influence of bigger storage volumes of the groundwater reservoir and a thick vadose zone, but also intense mixing of water in the riparian zones, diverse runoff generation processes and variable connectivity in the hillslopes.

The presented method is flexible in that it can be applied in various climates and soils and using various soil physical models. The estimated travel time estimates for the unsaturated zone have the potential for applications for solute transport and water quality issues, as shown by *Sprenger et al*. [2016]. Further, soil water isotope data have already been considered to test a catchment model [*Birkel et al*., 2014], but vadose zone travel times as derived in our study have not yet been applied to constrain or benchmark catchment models. New developments that enable us to efficiently analyze the pore water stable isotope signal in the laboratory or in situ [*Herbstritt et al*., 2012; *Volkmann and Weiler*, 2014] will allow us to trace precipitation through the vadose zone at higher spatiotemporal resolution. Thus, the time variable character of the percolation and root water uptake processes can potentially be monitored in the field in more detail. However, sufficient replications of such investigations are needed to decipher the influence of the soil type and meteorological forcing.

Acknowledgments
The study was funded by the DFG Research Group: From Catchments as Organised Systems to Models based on Functional Units (FOR 1598). We thank Liya Sun of the BOKU Vienna for providing LAI data for the grassland in the Attert catchment, Conrad Jackisch for providing soil physical parameters derived in the laboratory, Sibylle Hassler, Britta Kattenstroth, Begona Lorente Sistiaga, and Andrea Popp for LAI measurements, Begona Lorente Sistiaga, Andrea Popp, André Böker, Tyler Weiglein, Nikos Anestis, Marvin Reich, Benjamin Gralher, and Benjamin Müller for the help in the pore water isotope sampling. The fortnightly isotope data in the precipitation were provided by the FNR/CORE/SOWAT project of the Luxembourg Institute of Science and Technology—LIST. Special thanks to Britta Kattenstroth for her technical support in the field, Jeff Iffly for organizing landowner permits, the landowners for their permissions and Barbara Herbstritt for her support in the laboratory. The data are available upon request from the corresponding author. We thank three referees and the associate editor, Luis Samaniego, for reviewing the manuscript.

References

Ad-hoc-Arbeitsgruppe Boden (2005), *Bodenkundliche Kartieranleitung*, 5th ed., 438pp., Schweizerbart, Stuttgart.
Adomako, D., P. Maloszewski, C. Stumpp, S. Osae, and T. T. Akiti (2010), Estimating groundwater recharge from water isotope (δ^2H, δ^{18}O) depth profiles in the Densu River basin, Ghana, *Hydrol. Sci. J.*, *55*(8), 1405–1416, doi:10.1080/02626667.2010.527847.
Ali, M., A. Fiori, and D. Russo (2014), A comparison of travel-time based catchment transport models, with application to numerical experiments, *J. Hydrol.*, *511*, 605–618, doi:10.1016/j.jhydrol.2014.02.010.
Allen, S. T., J. R. Brooks, R. F. Keim, B. J. Bond, and J. J. McDonnell (2014), The role of pre-event canopy storage in throughfall and stemflow by using isotopic tracers, *Ecohydrology*, *7*(2), 858–868, doi:10.1002/eco.1408.
Allison, G. B., C. Barnes, C. M. Hughes, and F. Leaney (1984), Effect of climate and vegetation on oxygen-18 and deuterium profiles in soils, in *Isotope Hydrology 1983*, edited by IAEA, pp. 105–122, IAEA, Vienna.
Asano, Y., T. Uchida, and N. Ohte (2002), Residence times and flow paths of water in steep unchannelled catchments, Tanakami, Japan, *J. Hydrol.*, *261*(1–4), 173–192, doi:10.1016/S0022-1694(02)00005-7.
Bariac, T., C. Jusserand, and A. Mariotti (1990), Evolution spatio-temporelle de la composition isotopique de l'eau dans le continuum sol-plante-atmosphere, *Geochim. Cosmochim. Acta*, *54*(2), 413–424, doi:10.1016/0016-7037(90)90330-N.
Benettin, P., A. Rinaldo, and G. Botter (2013a), Kinematics of age mixing in advection-dispersion models, *Water Resour. Res.*, *49*, 8539–8551, doi:10.1002/2013WR014708.
Benettin, P., Y. van der Velde, S. E. A. T. M. van der Zee, A. Rinaldo, and G. Botter (2013b), Chloride circulation in a lowland catchment and the formulation of transport by travel time distributions, *Water Resour. Res.*, *49*, 4619–4632, doi:10.1002/wrcr.20309.
Benettin, P., J. W. Kirchner, A. Rinaldo, and G. Botter (2015a), Modeling chloride transport using travel time distributions at Plynlimon, Wales, *Water Resour. Res.*, *51*, 3259–3276, doi:10.1002/2014WR016600.
Benettin, P., A. Rinaldo, and G. Botter (2015b), Tracking residence times in hydrological systems: Forward and backward formulations, *Hydrol. Processes*, *29*(25), 5203–5213, doi:10.1002/hyp.10513.
Bertrand, G., J. Masini, N. Goldscheider, J. Meeks, V. Lavastre, H. Celle-Jeanton, J.-M. Gobat, and D. Hunkeler (2014), Determination of spatio-temporal variability of tree water uptake using stable isotopes (δ^{18}O, δ^2H) in an alluvial system supplied by a high-altitude watershed, Pfyn forest, Switzerland, *Ecohydrology*, *7*(2), 319–333, doi:10.1002/eco.1347.
Birkel, C., C. Soulsby, and D. Tetzlaff (2015), Conceptual modelling to assess how the interplay of hydrological connectivity, catchment storage and tracer dynamics controls nonstationary water age estimates, *Hydrol. Processes*, *29*(13), 2956–2969, doi:10.1002/hyp.10414.
Birkel, C., C. Soulsby, and D. Tetzlaff (2014), Developing a consistent process-based conceptualization of catchment functioning using measurements of internal state variables, *Water Resour. Res.*, *50*(4), 3481–3501, doi:10.1002/2013WR014925.
Birkel, C., C. Soulsby, D. Tetzlaff, S. Dunn, and L. Spezia (2012), High-frequency storm event isotope sampling reveals time-variant transit time distributions and influence of diurnal cycles, *Hydrol. Processes*, *26*(2), 308–316, doi:10.1002/hyp.8210.
Botter, G. (2012), Catchment mixing processes and travel time distributions, *Water Resour. Res.*, *48*, W05545, doi:10.1029/2011WR011160.
Botter, G., E. Bertuzzo, and A. Rinaldo (2010), Transport in the hydrologic response. Travel time distributions, soil moisture dynamics, and the old water paradox, *Water Resour. Res.*, *46*, W03514, doi:10.1029/2009WR008371.
Brand, W. A., H. Geilmann, E. R. Crosson, and C. W. Rella (2009), Cavity ring-down spectroscopy versus high-temperature conversion isotope ratio mass spectrometry; a case study on δ2H and δ18O of pure water samples and alcohol/water mixtures, *Rapid Commun. Mass Spectrom.*, *23*(12), 1879–1884, doi:10.1002/rcm.4083.
Brodersen, C., S. Pohl, M. Lindenlaub, C. Leibundgut, and K. V. Wilpert (2000), Influence of vegetation structure on isotope content of throughfall and soil water, *Hydrol. Processes*, *14*(8), 1439–1448, doi:10.1002/1099-1085(20000615)14:8 < 1439::aid-hyp985 > 3.0.CO;2-3.
Colbach, R., and R. Maquil (2003), *Carte géologique du Luxembourg 1/25000-Feuille n° 7 Rédange*, Service Géologique du Luxembourg, Luxembourg.
Craig, H., L. I. Gordon, and Y. Horibe (1963), Isotopic exchange effects in the evaporation of water. 1: Low-temperature experimental results, *J. Geophys. Res.*, *68*(17), 5079–5087, doi:10.1029/JZ068i017p05079.
Evaristo, J., S. Jasechko, and J. J. McDonnell (2015), Global separation of plant transpiration from groundwater and streamflow, *Nature*, *525*(7567), 91–94, doi:10.1038/nature14983.
Feddes, R. A., P. J. Kowalik, and H. Zaradny (1978), *Simulation of Field Water Use and Crop Yield, Simul. Monogr.*, 189 pp., Cent. for Agric. Publ. and Doc., Wageningen, Netherlands.
Gandomi, A. H., and A. H. Alavi (2012), Krill herd: A new bio-inspired optimization algorithm, *Commun. Nonlinear Sci. Numer. Simul.*, *17*(12), 4831–4845, doi:10.1016/j.cnsns.2012.05.010.
Gandomi, A. H., and A. H. Alavi (2016), An introduction of Krill Herd algorithm for engineering optimization, *J. Civil Eng. Manage.*, *22*(3), 302–310, doi:10.3846/13923730.2014.897986.
Garvelmann, J., C. Külls, and M. Weiler (2012), A porewater-based stable isotope approach for the investigation of subsurface hydrological processes, *Hydrol. Earth Syst. Sci.*, *16*(2), 631–640, doi:10.5194/hess-16-631-2012.
Geris, J., D. Tetzlaff, J. McDonnell, and C. Soulsby (2014), The relative role of soil type and tree cover on water storage and transmission in northern headwater catchments, *Hydrol. Processes*, *29*(7), 1844–1860, doi:10.1002/hyp.10289.
Godsey, S. E., et al. (2010), Generality of fractal 1/f scaling in catchment tracer time series, and its implications for catchment travel time distributions, *Hydrol. Processes*, *24*(12), 1660–1671, doi:10.1002/Hyp.7677.
Harman, C. J., and M. Kim (2014), An efficient tracer test for time-variable transit time distributions in periodic hydrodynamic systems, *Water Resour. Res.*, *41*(5), 1567–1575, doi:10.1002/2013GL058980.
Harman, C. J. (2015), Time-variable transit time distributions and transport: Theory and application to storage-dependent transport of chloride in a watershed, *Water Resour. Res.*, *51*, 1–30, doi:10.1002/2014WR015707.
Harman, C. J., P. S. C. Rao, N. B. Basu, G. S. McGrath, P. Kumar, and M. Sivapalan (2011), Climate, soil, and vegetation controls on the temporal variability of vadose zone transport, *Water Resour. Res.*, *47*, W00J13, doi:10.1029/2010WR010194.
Heidbüchel, I., P. A. Troch, S. W. Lyon, and M. Weiler (2012), The master transit time distribution of variable flow systems, *Water Resour. Res.*, *48*, W06520, doi:10.1029/2011WR011293.
Heidbüchel, I., P. A. Troch, and S. W. Lyon (2013), Separating physical and meteorological controls of variable transit times in zero-order catchments, *Water Resour. Res.*, *49*, 7644–7657, doi:10.1002/2012WR013149.
Herbstritt, B., B. Gralher, and M. Weiler (2012), Continuous in situ measurements of stable isotopes in liquid water, *Water Resour. Res.*, *48*, W03601, doi:10.1029/2011WR011369.
Hoffman, G., and M. van Genuchten (1983), Soil properties and efficient water use: Water management for salinity control, in *Limitations and Efficient Water Use in Crop Production*, edited by H. Taylor, W. Jordan, and T. Sinclair, pp. 73–85, Am. Soc. of Agron., Madison, Wis.

Hopmans, J. W., and M. T. van Genuchten (2005), Vadose zone: Hydrological processes, in *Encyclopedia of Soils in the Environment*, edited by D. Hillel, pp. 209–216, Elsevier, Amsterdam, Netherlands.
Hrachowitz, M., C. Soulsby, D. Tetzlaff, J. J. C. Dawson, S. M. Dunn, and I. A. Malcolm (2009a), Using long-term data sets to understand transit times in contrasting headwater catchments, *J. Hydrol.*, *367*(3–4), 237–248, doi:10.1016/j.jhydrol.2009.01.001.
Hrachowitz, M., C. Soulsby, D. Tetzlaff, J. J. C. Dawson, and I. A. Malcolm (2009b), Regionalization of transit time estimates in montane catchments by integrating landscape controls, *Water Resour Res.*, *45*, W05421, doi:10.1029/2008WR007496.
Hrachowitz, M., C. Soulsby, D. Tetzlaff, I. A. Malcolm, and G. Schoups (2010), Gamma distribution models for transit time estimation in catchments. Physical interpretation of parameters and implications for time-variant transit time assessment, *Water Resour Res.*, *46*, W10536, doi:10.1029/2010WR009148.
Hrachowitz, M., H. Savenije, T. A. Bogaard, D. Tetzlaff, and C. Soulsby (2013), What can flux tracking teach us about water age distribution patterns and their temporal dynamics?, *Hydrol. Earth Syst. Sci.*, *17*(2), 533–564, doi:10.5194/hess-17-533-2013.
Hu, K., H. Chen, Y. Nie, and K. Wang (2015), Seasonal recharge and mean residence times of soil and epikarst water in a small karst catchment of southwest China, *Sci. Rep.*, *5*, 10215, doi:10.1038/srep10215.
IUSS Working Group WRB (2006), *World Reference Base for Soil Resources 2006. A Framework for International Classification, Correlation and Communication*, World Soil Resour. Rep., Food and Agric. Organ. of the U. N., Rome.
Jarvis, N. J. (1994), The MACRO model (Version 3.1), Technical description and sample simulations, *Rep. and Diss. 9*, Dep. Soil Sci., Swedish Univ. Agric. Sci., Uppsala, Sweden.
Jasechko, S., S. J. Birks, T. Gleeson, Y. Wada, P. J. Fawcett, Z. D. Sharp, J. J. McDonnell, and J. M. Welker (2014), The pronounced seasonality of global groundwater recharge, *Water Resour. Res.*, *50*, 8845–8867, doi:10.1002/2014WR015809.
Juilleret, J., J. F. Iffly, L. Pfister, and C. Hissler (2011), Remarkable Pleistocene periglacial slope deposits in Luxembourg (Oesling): Pedological implication and geosite potential, *Bull. Société des Nat. Luxembourgeois (Bull. Soc. Nat. Luxemb.)*, *112*, 125–130.
Kabeya, N., M. Katsuyama, M. Kawasaki, N. Ohte, and A. Sugimoto (2007), Estimation of mean residence times of subsurface waters using seasonal variation in deuterium excess in a small headwater catchment in Japan, *Hydrol. Processes*, *21*(3), 308–322, doi:10.1002/hyp.6231.
Kabeya, N., A. Shimizu, K. Tamai, S. Iida, and T. Shimizu (2011), Transit times of soil water in thick soil and weathered gneiss layers using deuterium excess modelling, in *Proceedings of Symposium H01 held during IUGG2011, IAHS Publ.*, vol. 345, edited by IAHS, pp. 163–168, IAHS, Vienna.
Kim, S. (2014), Hydrometric transit times along transects on a steep hillslope, *Water Resour. Res.*, *50*, 7267–7284, doi:10.1002/2013WR014746.
Kim, S., and S. Jung (2014), Estimation of mean water transit time on a steep hillslope in South Korea using soil moisture measurements and deuterium excess, *Hydrol. Processes*, *28*(4), 1844–1857, doi:10.1002/hyp.9722.
Kirchner, J. W. (2016a), Aggregation in environmental systems—Part 1: Seasonal tracer cycles quantify young water fractions, but not mean transit times, in spatially heterogeneous catchments, *Hydrol. Earth Syst. Sci.*, *20*(1), 279–297, doi:10.5194/hess-20-279-2016.
Kirchner, J. W. (2016b), Aggregation in environmental systems—Part 2: Catchment mean transit times and young water fractions under hydrologic nonstationarity, *Hydrol. Earth Syst. Sci.*, *20*(1), 299–328, doi:10.5194/hess-20-299-2016.
Kirchner, J. W., X. H. Feng, and C. Neal (2001), Catchment-scale advection and dispersion as a mechanism for fractal scaling in stream tracer concentrations, *J. Hydrol.*, *254*(1–4), 82–101, doi:10.1016/S0022-1694(01)00487-5.
Kirchner, J. W., D. Tetzlaff, and C. Soulsby (2010), Comparing chloride and water isotopes as hydrological tracers in two Scottish catchments, *Hydrol. Processes*, *24*(12), 1631–1645, doi:10.1002/Hyp.7676.
Kling, H., M. Fuchs, and M. Paulin (2012), Runoff conditions in the upper Danube basin under an ensemble of climate change scenarios, *J. Hydrol.*, *424–425*, 264–277, doi:10.1016/j.jhydrol.2012.01.011.
Kudo, K., T. Nagamatsu, J. Shimada, N. Kabeya, and N. Tanaka (2013), Subsurface storage in different land use catchments evaluated by deuterium excess, in *Climate and Land Surface Changes in Hydrology, IAHS Publ.*, vol.359, edited by E. Boegh, E. Blyth, and D. M. Hannah, pp. 371–376, IAHS, Oxfordshire, U. K.
Lee, K.-S., J.-M. Kim, D.-R. Lee, Y. Kim, and D. Lee (2007), Analysis of water movement through an unsaturated soil zone in Jeju Island, Korea using stable oxygen and hydrogen isotopes, *J. Hydrol.*, *345*(3–4), 199–211, doi:10.1016/j.jhydrol.2007.08.006.
Lindström, G., and A. Rodhe (1992), Transit times of water in soil lysimeters from modeling of oxygen-18, *Water Air Soil Pollut.*, *65*(1–2), 83–100, doi:10.1007/BF00482751.
Majoube, M. (1971), Fractionnement en oxygene-18 et en deuterium entre l'eau et sa vapeur, *J. Chim. Phys.*, *68*(10), 1423–1436.
Maloszewski, P., S. Maciejewski, C. Stumpp, W. Stichler, P. Trimborn, and D. Klotz (2006), Modelling of water flow through typical Bavarian soils. 2: Environmental deuterium transport, *Hydrol. Sci. J.*, *51*(2), 298–313, doi:10.1623/hysj.51.2.298.
Martínez-Carreras, N., A. Krein, F. Gallart, J.-F. Iffly, C. Hissler, L. Pfister, L. Hoffmann, and P. N. Owens (2012), The influence of sediment sources and hydrologic events on the nutrient and metal content of fine-grained sediments (Attert River Basin, Luxembourg), *Water Air Soil Pollut.*, *223*(9), 5685–5705, doi:10.1007/s11270-012-1307-1.
McDonnell, J. J., and K. Beven (2014), Debates-The future of hydrological sciences: A (common) path forward? A call to action aimed at understanding velocities, celerities and residence time distributions of the headwater hydrograph, *Water Resour. Res.*, *50*, 5342–5350, doi:10.1002/2013WR015141.
McDonnell, J. J., et al. (2010), How old is streamwater? Open questions in catchment transit time conceptualization, modelling and analysis, *Hydrol. Processes*, *24*(12), 1745–1754, doi:10.1002/Hyp.7796.
McGuire, K. J., and J. J. McDonnell (2006), A review and evaluation of catchment transit time modeling, *J. Hydrol.*, *330*(3–4), 543–563, doi:10.1016/j.jhydrol.2006.04.020.
McGuire, K. J., and J. J. McDonnell (2010), Hydrological connectivity of hillslopes and streams. Characteristic time scales and nonlinearities, *Water Resour. Res.*, *46*, W10543, doi:10.1029/2010WR009341.
McGuire, K. J., M. Weiler, and J. J. McDonnell (2007), Integrating tracer experiments with modeling to assess runoff processes and water transit times, *Adv. Water Resour.*, *30*(4), 824–837, doi:10.1016/j.advwatres.2006.07.004.
McMillan, H., D. Tetzlaff, M. Clark, and C. Soulsby (2012), Do time-variable tracers aid the evaluation of hydrological model structure? A multimodel approach, *Water Resour. Res.*, *48*, W05501, doi:10.1029/2011WR011688.
Meinen, C., D. Hertel, and C. Leuschner (2009), Biomass and morphology of fine roots in temperate broad-leaved forests differing in tree species diversity: Is there evidence of below-ground overyielding?, *Oecologia*, *161*(1), 99–111, doi:10.1007/s00442-009-1352-7.
Mertens, J., R. Stenger, and G. F. Barkle (2006), Multiobjective inverse modeling for soil parameter estimation and model verification, *Vadose Zone J.*, *5*(3), 917–933, doi:10.2136/vzj2005.0117.
Millington, R. J., and J. P. Quirk (1961), Permeability of porous solids, *Trans. Faraday Soc.*, *57*, 1200–1207, doi:10.1039/TF9615701200.

Mills, R. (1973), Self-diffusion in normal and heavy water in the range 1-45.deg, *J. Phys. Chem.*, *77*(5), 685–688, doi:10.1021/j100624a025.
Mualem, Y. (1976), A new model for predicting the hydraulic conductivity of unsaturated porous media, *Water Resour. Res.*, *12*(3), 513–522, doi:10.1029/WR012i003p00513.
Mueller, M. H., A. Alaoui, C. Kuells, H. Leistert, K. Meusburger, C. Stumpp, M. Weiler, and C. Alewell (2014), Tracking water pathways in steep hillslopes by $\delta^{18}O$ depth profiles of soil water, *J. Hydrol.*, *519*, 340–352, doi:10.1016/j.jhydrol.2014.07.031.
Muñoz-Villers, L. E., and J. J. McDonnell (2012), Runoff generation in a steep, tropical montane cloud forest catchment on permeable volcanic substrate, *Water Resour. Res.*, *48*, W09528, doi:10.1029/2011WR011316.
Nimmo, J. R. (2007), Simple predictions of maximum transport rate in unsaturated soil and rock, *Water Resour. Res.*, *43*, W05426, doi:10.1029/2006WR005372.
Orlowski, N., L. Breuer, and J.J. McDonnell (2016), Critical issues with cryogenic extraction of soil water for stable isotope analysis, *Ecohydrology*, *9*, 3–10, doi:10.1002/eco.1722.
Peralta-Tapia, A., R. A. Sponseller, D. Tetzlaff, C. Soulsby, and H. Laudon (2014), Connecting precipitation inputs and soil flow pathways to stream water in contrasting boreal catchments, *Hydrol. Processes*, *29*(16), 3546–3555, doi:10.1002/hyp.10300.
Qu, W., H. R. Bogena, J. A. Huisman, J. Vanderborght, M. Schuh, E. Priesack, and H. Vereecken (2015), Predicting subgrid variability of soil water content from basic soil information, *Geophys. Res. Lett.*, *42*(3), 789–796, doi:10.1002/2014GL062496.
Queloz, P., E. Bertuzzo, L. Carraro, G. Botter, F. Miglietta, P. S. C. Rao, and A. Rinaldo (2015a), Transport of fluorobenzoate tracers in a vegetated hydrologic control volume: 1. Experimental results, *Water Resour. Res.*, *51*, 2773–2792, doi:10.1002/2014WR016433.
Queloz, P., L. Carraro, P. Benettin, G. Botter, A. Rinaldo, and E. Bertuzzo (2015b), Transport of fluorobenzoate tracers in a vegetated hydrologic control volume: 2. Theoretical inferences and modeling, *Water Resour. Res.*, *51*, 2793–2806, doi:10.1002/2014WR016508.
Raviv, M., and J. H. Lieth (2008), *Soilless Culture: Theory and Practice: Theory and Practice*, Elsevier, Amsterdam, Netherlands.
Rinaldo, A., K. J. Beven, E. Bertuzzo, L. Nicotina, J. Davies, A. Fiori, D. Russo, and G. Botter (2011), Catchment travel time distributions and water flow in soils, *Water Resour. Res.*, *47*, W05421, doi:10.1029/2011WR010478.
Rinaldo, A., P. Benettin, C. Harman, M. Hrachowitz, K. McGuire, Y. van der Velde, E. Bertuzzo, and G. Botter (2015), Storage selection functions: A coherent framework for quantifying how catchments store and release water and solutes, *Water Resour. Res.*, *51*, 4840–4847, doi:10.1002/2015WR017273.
Rodhe, A., L. Nyberg, and K. Bishop (1996), Transit times for water in a small till catchment from a step shift in the Oxygen 18 content of the water input, *Water Resour. Res.*, *32*(12), 3497–3511, doi:10.1029/95WR01806.
Sayama, T., and J. J. McDonnell (2009), A new time-space accounting scheme to predict stream water residence time and hydrograph source components at the watershed scale, *Water Resour. Res.*, *45*, W07401, doi:10.1029/2008WR007549.
Schaap, M. G., F. J. Leij, and M. T. van Genuchten (2001), ROSETTA: A computer program for estimating soil hydraulic parameters with hierarchical pedotransfer functions, *J. Hydrol.*, *251*(3–4), 163–176, doi:10.1016/S0022-1694(01)00466-8.
Schwärzel, K., A. Menzer, F. Clausnitzer, U. Spank, J. Häntzschel, T. Grünwald, B. Köstner, C. Bernhofer, and K.-H. Feger (2009), Soil water content measurements deliver reliable estimates of water fluxes: A comparative study in a beech and a spruce stand in the Tharandt forest (Saxony, Germany), *Agric. For. Meteorol.*, *149*(11), 1994–2006, doi:10.1016/j.agrformet.2009.07.006.
Seeger, S., and M. Weiler (2014), Lumped convolution integral models revisited: On the meaningfulness of inter catchment comparisons, *Hydrol. Earth Syst. Sci.*, *18*, 4751–4771, doi:10.5194/hess-18-4751-2014.
Shaw, S. B., A. A. Harpold, J. C. Taylor, and M. T. Walter (2008), Investigating a high resolution, stream chloride time series from the Biscuit Brook catchment, Catskills, NY, *J. Hydrol.*, *348*(3–4), 245–256, doi:10.1016/j.jhydrol.2007.10.009.
Šimůnek, J., M. Sejna, H. Saito, M. Sakai, and M. Th. van Genuchten (2012), *The HYDRUS-1D Software Package for Simulating the One-Dimensional Movement of Water, Heat, and Multiple Solutes in Variably-Saturated Media, Version 4.15*, Dep. of Environ. Sci., Univ. of Calif., Riverside, Calif.
Sprenger, M., B. Herbstritt, and M. Weiler (2015a), Established methods and new opportunities for pore water stable isotope analysis, *Hydrol. Processes*, *29*(25), 5174–5192, doi:10.1002/hyp.10643.
Sprenger, M., T. H. M. Volkmann, T. Blume, and M. Weiler (2015b), Estimating flow and transport parameters in the unsaturated zone with pore water stable isotopes, *Hydrol. Earth Syst. Sci.*, *19*(6), 2617–2635, doi:10.5194/hess-19-2617-2015.
Sprenger, M., M. Erhardt, M. Riedel, and M. Weiler (2016), Historical tracking of nitrate in contrasting vineyards using water isotopes and nitrate depth profiles, *Agric. Environ. Ecol.*, *222*, 185–192, doi:10.1016/j.agee.2016.02.014
Stewart, M. K., and J. J. McDonnell (1991), Modeling base-flow soil-water residence times from deuterium concentrations, *Water Resour. Res.*, *27*(10), 2681–2693, doi:10.1029/91WR01569.
Stewart, M. K., J. Mehlhorn, and S. Elliott (2007), Hydrometric and natural tracer (oxygen-18, silica, tritium and sulphur hexafluoride) evidence for a dominant groundwater contribution to Pukemanga Stream, New Zealand, *Hydrol. Processes*, *21*(24), 3340–3356, doi:10.1002/hyp.6557.
Stumpp, C., and M. J. Hendry (2012), Spatial and temporal dynamics of water flow and solute transport in a heterogeneous glacial till: The application of high-resolution profiles of $\delta^{18}O$ and $\delta^{2}H$ in pore waters, *J. Hydrol.*, *438–439*, 203–214, doi:10.1016/j.jhydrol.2012.03.024.
Stumpp, C., G. Nützmann, S. Maciejewski, and P. Maloszewski (2009), A comparative modeling study of a dual tracer experiment in a large lysimeter under atmospheric conditions, *J. Hydrol.*, *375*(3–4), 566–577, doi:10.1016/j.jhydrol.2009.07.010.
Stumpp, C., W. Stichler, M. Kandolf, and J. Šimůnek (2012), Effects of land cover and fertilization method on water flow and solute transport in five lysimeters: A long-term study using stable water isotopes, *Vadose Zone J.*, *11*(1), vzj2011.0075, doi:10.2136/vzj2011.0075.
Tetzlaff, D., C. Birkel, J. Dick, J. Geris, and C. Soulsby (2014), Storage dynamics in hydropedological units control hillslope connectivity, runoff generation and the evolution of catchment transit time distributions, *Water Resour. Res.*, *50*, 969–985, doi:10.1002/2013WR014147.
Timbe, E., D. Windhorst, P. Crespo, H.-G. Frede, J. Feyen, and L. Breuer (2014), Understanding uncertainties when inferring mean transit times of water trough tracer-based lumped-parameter models in Andean tropical montane cloud forest catchments, *Hydrol. Earth Syst. Sci.*, *18*(4), 1503–1523, doi:10.5194/hess-18-1503-2014.
van der Velde, Y., G. H. de Rooij, J. C. Rozemeijer, F. C. van Geer, and H. P. Broers (2010), Nitrate response of a lowland catchment: On the relation between stream concentration and travel time distribution dynamics, *Water Resour. Res.*, *46*, W11534, doi:10.1029/2010WR009105.
van der Velde, Y., P. J. J. F. Torfs, S. E. A. T. M. van der Zee, and R. Uijlenhoet (2012), Quantifying catchment-scale mixing and its effect on time-varying travel time distributions, *Water Resour. Res.*, *48*, W06536, doi:10.1029/2011WR011310.
van der Velde, Y., I. Heidbüchel, S. W. Lyon, L. Nyberg, A. Rodhe, K. Bishop, and P. A. Troch (2015), Consequences of mixing assumptions for time-variable travel time distributions, *Hydrol. Processes*, *29*(16), 3460–3474, doi:10.1002/hyp.10372.
van Genuchten, M. T. (1980), A closed-form equation for predicting the hydraulic conductivity of unsaturated soils, *Soil Sci. Soc. Am. J.*, *44*(5), 892–898.

Vanderborght, J., and H. Vereecken (2007), Review of dispersivities for transport modeling in soils, *Vadose Zone J.*, *6*(1), 29–52, doi:10.2136/vzj2006.0096.

Vereecken, H., T. Kamai, T. Harter, R. Kasteel, J. Hopmans, and J. Vanderborght (2007), Explaining soil moisture variability as a function of mean soil moisture: A stochastic unsaturated flow perspective, *Geophys. Res. Lett.*, *34*, L22402, doi:10.1029/2007GL031813.

Volkmann, T. H. M., and M. Weiler (2014), Continual in-situ monitoring of pore water stable isotopes in the subsurface, *Hydrol. Earth Syst. Sci.*, *18*, 1819–1833, doi:10.5194/hess-18-1819-2014.

Vrugt, J., W. Bouten, and A. Weerts (2001), Information content of data for identifying soil hydraulic parameters from outflow experiments, *Soil Sci. Soc. Am. J.*, *65*(1), 19–27, doi:10.2136/sssaj2001.65119x.

Vuichard, N., P. Ciais, N. Viovy, P. Calanca, and J.-F. Soussana (2007), Estimating the greenhouse gas fluxes of European grasslands with a process-based model. 2: Simulations at the continental level, *Global Biogeochem. Cycles*, *21*, GB1005, doi:10.1029/2005GB002612.

Wang, G., L. Guo, A. H. Gandomi, L. Cao, A. H. Alavi, H. Duan, and J. Li (2013), Lévy-Flight Krill Herd Algorithm, *Math. Prob. Eng.*, *2013*(6), 1–14, doi:10.1155/2013/682073.

Wang, P., X. Song, D. Han, Y. Zhang, and X. Liu (2010), A study of root water uptake of crops indicated by hydrogen and oxygen stable isotopes: A case in Shanxi Province, China, *Agric. Water Manage.*, *97*(3), 475–482, doi:10.1016/j.agwat.2009.11.008.

Wang, Q., J. Tenhunen, A. Granier, M. Reichstein, O. Bouriaud, D. Nguyen, and N. Breda (2004), Long-term variations in leaf area index and light extinction in a Fagus sylvatica stand as estimated from global radiation profiles, *Theor. Appl. Climatol.*, *79*(3–4), 225–238, doi:10.1007/s00704-004-0074-3.

Wassenaar, L., M. Hendry, V. Chostner, and G. Lis (2008), High resolution pore water δ^2H and δ^{18}O measurements by H_2O (liquid)−H_2O (vapor) equilibration laser spectroscopy, *Environ. Sci. Technol.*, *42*(24), 9262–9267, doi:10.1021/es802065s.

Weiler, M., and F. Naef (2003), An experimental tracer study of the role of macropores in infiltration in grassland soils, *Hydrol. Processes*, *17*(2), 477–493, doi:10.1002/Hyp.1136.

Weiler, M., and J. McDonnell (2004), Virtual experiments: A new approach for improving process conceptualization in hillslope hydrology, *J. Hydrol.*, *285*(1–4), 3–18, doi:10.1016/S0022-1694(03)00271-3.

Weiler, M., and J. J. McDonnell (2007), Conceptualizing lateral preferential flow and flow networks and simulating the effects on gauged and ungauged hillslopes, *Water Resour. Res.*, *43*, W03403, doi:10.1029/2006WR004867.

Wesseling, J. G. (1991), Meerjarige simulaties van gronwateronttrekking voor verschillende bodmprofielen, grondwatertrappen en gewassen met het model SWATRE, *Rep. 152*, Wageningen, Netherlands.

Wessolek, G., M. Kaupenjohann, and M. Renger (Eds.) (2009), *Bodenphysikalische Kennwerte und Berechnungsverfahren für die Praxis*, Bodenökologie und Bodengenese Heft 40 40, Tech. Univ. Berlin Selbstverlag, Berlin, Germany.

West, A. G., G. R. Goldsmith, P. D. Brooks, and T. E. Dawson (2010), Discrepancies between isotope ratio infrared spectroscopy and isotope ratio mass spectrometry for the stable isotope analysis of plant and soil waters, *Rapid Commun. Mass Spectrom.*, *24*(14), 1948–1954, doi:10.1002/rcm.4597.

Wittmann, O., H.-P. Blume, and M. Filipinski (1997), Soil classification of the Federal Republic of Germany, *Working Group on Soil Classification of the German Soil Science Society, Mitt. Dtsch. Bodenk. Ges.*, *84*, 253–275.

Wrede, S., F. Fenicia, N. Martínez-Carreras, J. Juilleret, C. Hissler, A. Krein, H. H. G. Savenije, S. Uhlenbrook, D. Kavetski, and L. Pfister (2015), Towards more systematic perceptual model development: A case study using 3 Luxembourgish catchments, *Hydrol. Processes*, *29*(12), 2731–2750, doi:10.1002/hyp.10393.

Zimmermann, U., D. Ehhalt, and K. Münnich (1967), Soil-water movement and evapotranspiration: Changes in the isotopic composition of the water, in *Isotopes in hydrology*, edited by IAEA, pp. 567–585, Int. At. Energy Agency, Vienna.

Zuber, A., and P. Małoszewski (2001), Lumped parameter models, in *Environmental Isotopes in the Hydrological Cycle Principles and Applications*, edited by W.G. Mook, pp. 5–35, Int. At. Energy Agency, Vienna.